ADVANCED FUNCTIONAL MATERIALS
www.afm-journal.de

A Library of Late Transition Metal Alloy Dielectric Functions for Nanophotonic Applications

J. Magnus Rahm, Christopher Tiburski, Tuomas P. Rossi, Ferry Anggoro Ardy Nugroho, Sara Nilsson, Christoph Langhammer, and Paul Erhart**

Accurate complex dielectric functions are critical to accelerate the development of rationally designed metal alloy systems for nanophotonic applications, and to thereby unlock the potential of alloying for tailoring nanostructure optical properties. To date, however, accurate alloy dielectric functions are widely lacking. Here, a time-dependent density-functional theory computational framework is employed to compute a comprehensive binary alloy dielectric function library for the late transition metals most commonly employed in plasmonics (Ag, Au, Cu, Pd, Pt). Excellent agreement is found between electrodynamic simulations based on these dielectric functions and selected alloy systems experimentally scrutinized in 10 at% composition intervals. Furthermore, it is demonstrated that the dielectric functions can vary in very non-linear fashion with composition, which paves the way for non-trivial optical response optimization by tailoring material composition. The presented dielectric function library is thus a key resource for the development of alloy nanomaterials for applications in nanophotonics, optical sensors, and photocatalysis.

1. Introduction

In many fields of science and technology, properties and functionalities of materials are engineered and optimized by combining multiple chemical species. Steel, for example, is reinforced by mixing carbon into an iron matrix, or made "stainless" by adding elements such as Ni and Cr. Other more recent examples include Pt alloys with Ni, Fe, or rare earth metals that significantly improve and lower the cost of fuel cell catalysts.[1] These examples illustrate that in materials science and engineering, alloying is often the most powerful tool for tailoring and optimizing material properties and functionality. In nanooptics and plasmonics, however, which over the last decade emerged as one of the most dynamic research areas in nanoscience, this concept is still in its infancy. The impressive development of the plasmonics field has rather occurred almost exclusively on the basis of a single platform, namely nanostructures of pure gold. It was not until very recently, enabled by the development of the corresponding nanofabrication methods, that systematic investigations of the fundamental properties of noble metal alloy nanostructures started to appear.[2–10] Some of these materials have already found applications, for example in plasmonic hydrogen sensors,[11,12] or are suggested for the use in plasmon-mediated catalysis.[13]

Despite these successful initial efforts in establishing alloying as a new handle for tailoring the optical properties of metal nanoparticles, the bottlenecks of this emerging field are the lack of fundamental understanding of the optical properties of alloys at the atomic level, as well as the limited availability of reliable complex dielectric functions (DFs) of metal alloys across a wide composition range, with exceptions focusing mainly on the Ag–Au system[7,14,15] and a few other alloys.[16–18] The availability of DFs is particularly important because they are the critical ingredient for any type of electrodynamic simulations, which are widely and very effectively used for predicting the response and optimizing the design of nanophotonic structures.[19,20] At the same time, the experimental determination of DFs in the UV–vis–NIR spectral range is unfortunately both cumbersome and prone to significant errors, as apparent from a survey of literature data for pure Au, arguably the chemically most stable element under ambient conditions (Figure S1b, Supporting Information, and references therein). One can therefore expect this task to be even more difficult for any other metal. The observed spread in experimental data is caused, for example, by different processing parameters used during film growth,[20] differences in surface roughness, morphology, film/sample thickness, as well as impurities,[21] different techniques employed to measure the optical spectra, and eventually the inversion of these data to obtain the DF.[22] When metals prone to oxidation are included, experimental uncertainties are accentuated further due to the risk of both surface/bulk oxidation and oxidation along grain boundaries.[23] Moreover, one must consider surface segregation of alloyants,[24] which itself is sensitive to adsorption of species from the environment, depending on, for example, their reduction or oxidation potential.[25] Finally, also experimental control and post-fabrication determination of

J. M. Rahm, C. Tiburski, Dr. T. P. Rossi, Dr. F. A. A. Nugroho, S. Nilsson, Prof. C. Langhammer, Prof. P. Erhart
Department of Physics
Chalmers University of Technology
Gothenburg S-412 96, Sweden
E-mail: clangham@chalmers.se; erhart@chalmers.se

The ORCID identification number(s) for the author(s) of this article can be found under https://doi.org/10.1002/adfm.202002122.

DOI: 10.1002/adfm.202002122

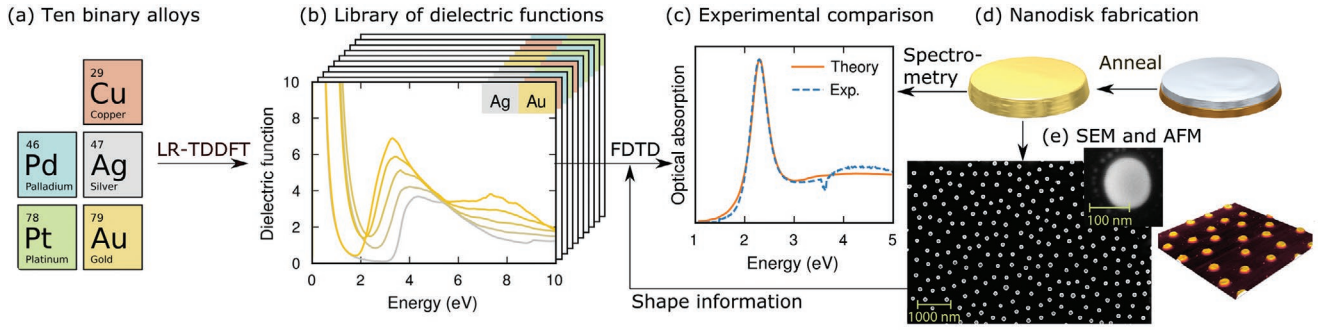

Figure 1. Methodological overview. a) Ten binary alloys of Cu, Pd, Ag, Pt, and Au were analyzed with LR-TDDFT to create a b) comprehensive library of dielectric functions. A subset of these dielectric functions was then used in FDTD simulations to compute c) the optical response of single alloy nanodisks (in this case 50 at% Ag–Au). These extinction spectra were compared to corresponding experimental data obtained from quasi-random arrays of d) alloy nanodisks, nanofabricated onto transparent substrates. Representative SEM and AFM images of experimentally obtained 50 at% Au–Pd nanodisk arrays are displayed in panel (e). The inset displays an SEM image of a single $Au_{20}Cu_{80}$ nanodisk.

alloy composition are prone to uncertainties in the at% range, and for a detailed mapping of the optical properties as a function of composition a large number of samples is required, which can be challenging to produce in a reproducible and consistent way.

In response, here, we present a comprehensive library of DFs obtained by first-principles calculations based on linear-response time-dependent density-functional theory (LR-TDDFT)[26] for ten binary alloys composed of the late non-magnetic transition elements Pd, Pt, Cu, Ag, and Au (**Figure 1**a,b). This approach, which has previously been applied primarily to monoelemental systems,[27] compounds with small unit cells,[28] semiconductor alloys,[29] and hydrogenated Pd,[30,31] directly yields the DF over the full spectral range. Although LR-TDDFT is not exact, with the most important approximations pertaining to the exchange-correlation functional, it enables efficient and systematic screening of different alloys and compositions and is thus well suited for building a self-consistent library of DFs. In addition, the computational approach provides control over the chemical ordering, that is, how the elements are distributed over the lattice at the atomic level. This allows us to systematically investigate how the DFs of random alloys compare with ordered structures, in particular the intermetallic phases that appear at specific compositions in the phase diagram of several of these alloy systems. It should be noted, however, that the relatively high computational cost of LR-TDDFT puts a limit to the system sizes (number of atoms per unit cell) that can be treated, which for metallic alloys translates to a restriction on what degrees of chemical order can be probed. In particular, fully random alloys cannot be calculated with LR-TDDFT, but can be well approximated using so-called special quasi-random structure (SQS).[32]

To rigorously benchmark experimentally our first principles framework and the calculated DFs, we nanofabricated quasi-random arrays of nanodisks using hole-mask colloidal lithography[3,33] for four different rationally selected alloy systems (Ag–Au, Au–Pd, Au–Cu, Ag–Pd) with 10 at% composition intervals, for which we systematically measured the plasmonic response. Comparing the experimentally determined plasmonic resonance peak descriptors spectral position and full width at half maximum (FWHM) with finite-difference time-domain (FDTD) electrodynamic simulations using the DFs obtained by first-principles calculations as input (Figure 1c–e), we find excellent agreement and thus validate our approach. Furthermore, the results reveal strongly non-trivial changes in the DF with composition with the degree of non-linearity being very sensitive to wavelength. In combination with nanoparticle shape (and size) this leads to a non-trivial composition dependence of the optical response, as observed also in the experiments. On a fundamental level, the features of the DF can be qualitatively related to the density of states (DOS) and in particular the position of the d-band edge. The combination of DFs from first-principles calculations with FDTD simulations thus provides a powerful platform for designing optical alloy materials in general and for alloy plasmonics in particular. In this spirit, we have made the data underlying the present study available via a web application (https://sharc.materialsmodeling.org/alloy_dielectric_functions/) that enables convenient and rapid access for theoreticians and experimentalists alike.

2. Results and Discussion

2.1. Pure Elements

Before delving into alloys, we verify the fundamental reliability of our computational framework by assessing the DFs of the pure elements of interest here, that is, Ag, Au, Cu, Pd, and Pt (see Section 4 for computational details). The agreement between our calculated DFs and available experimental data is generally good (Figures S1 and S2, Supporting Information). However, it is also very important to emphasize the large variations in the experimental data and the large number of different measurements and techniques that are required to span the entire spectral range considered in our calculations. This in turn highlights one of the key problems to date, namely that it is merely impossible to find and employ a complete and consistent DF data set for the predictive computation of alloy nanostructure optical properties.

As a second aspect, we highlight that a particularly important feature for the plasmonic response of the late transition metal alloys is the energy at which the imaginary part of the DF increases due to the onset of interband transitions from the

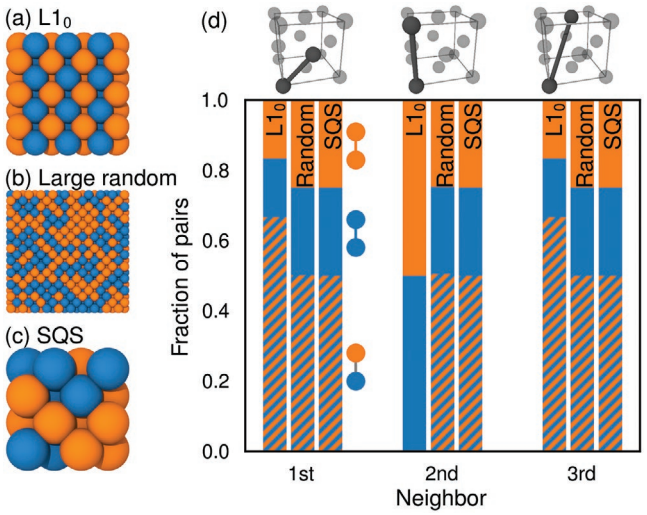

Figure 2. Alloys exhibit various degrees of order, spanning from ordered intermetallic phases such as a) $L1_0$, to b) completely random. Order can be characterized by d) pair correlations, that is, the fraction of nearest neighbor pairs (1st, 2nd, 3rd, etc.) that are unlike (blue–orange) and alike (blue–blue and orange–orange). For example, 2/3 of the first nearest neighbor pairs in the $L1_0$ structure are blue–orange, while 1/3 are blue–blue or orange–orange. Large random structures at 50% concentration have 1/2 of its neighboring pairs (of any order) blue–orange, 1/4 blue–blue, and 1/4 orange–orange. The $L1_0$ structure can be represented by a unit cell with only two atoms, and is thus feasible to treat with LR-TDDFT. The large, random structure, on the other hand, is in general too large to be computed with LR-TDDFT. c) SQSs reproduce the pair correlations of large, random alloys using much smaller unit cells that are computationally tractable. SQSs are thus excellent models for random alloys in computationally relatively expensive methods such as LR-TDDFT.

d-band. Also in this regard, our calculations agree very well with experimental data, with only a very slight under and overestimation in the case of Ag and Cu, respectively. The good performance can be largely attributed to the self-consistent version of the exchange-correlation functional by Gritsenko, van Leeuwen, van Lenthe, and Baerends (GLLB-sc),[34,35] which accurately describes the position of the d-band without resorting to empirical parameters unlike, for example, in the DFT+U approach.

2.2. Alloys

We start the analysis of alloys with **Ag–Au**, which is arguably the most widely studied alloy with regard to optical properties. Ag–Au is expected to form a substitutional random alloy in the full concentration range.[36] Here, we use SQSs to model the disorder,[32] since they allow us to represent the random alloy in modestly sized supercells, keeping the system sizes manageable for LR-TDDFT calculations (**Figure 2**; see also Section 4 for more details; atomic structures are provided in the Supporting Information). As the first conclusion for the calculated DF of the Ag–Au system, we find that their dependency on concentration is not entirely linear, but can can be reasonably well approximated as such (**Figure 3**a; see also Figures S4a and S5a, Supporting Information). This is in qualitative agreement with previous experimental studies (Figure S8, Supporting Information), but just as in the case of the pure elements, the available literature exhibits considerable quantitative variation. We emphasize also that the deviation from non-linearity, although it appears small, may yet be consequential for the optical response of certain systems.[37–39]

Next, we assess how well the calculated Ag–Au DFs perform when used for FDTD simulations of the plasmonic response of Ag–Au nanodisks, which we nanofabricated in quasi-random arrays across the full range of composition and assessed experimentally by measuring their extinction spectra. Furthermore, we confirmed homogeneous alloy formation using both scanning transmission electron microscopy (STEM) with energy-dispersive X-ray spectroscopy (EDS) and X-ray photoelectron spectroscopy (XPS) analysis (**Figure 4**; Figure S15, Supporting Information). Since the optical extinction spectra of such nanostructures are sensitive not only to alloy composition but also to the aspect ratio of the disk (Figure S3, Supporting Information), we first measured the diameter and height of the nanofabricated disks for each alloy composition using scanning electron microscopy (SEM) and atomic force microscopy (AFM) (Figure S14, Supporting Information), and then used the obtained dimensions in the corresponding FDTD simulations. For the comparison between experiment and FDTD simulations, we extracted the FWHM and spectral peak position from the experimentally measured and computed optical extinction spectra (Figure S16, Supporting Information). We find excellent agreement between the two throughout the entire range of compositions and with very small variation, in line with the low variations of DF with composition in this system (Figure 4a).[40]

Next, we consider the **Au–Cu** system, which unlike Ag–Au exhibits intermetallic phases at certain alloy compositions. Nevertheless, we first consider only a random alloy with random chemical order modeled using SQS and find that the corresponding composition dependence of the calculated DF is weak (Figure 3b; Figure S5b, Supporting Information) and in good agreement with previous literature (Figure S9, Supporting Information). To also investigate the impact of chemical ordering on DFs, and eventually on the simulated optical extinction spectra of nanodisks comprised of an intermetallic phase rather than a random alloy, we also calculated the DFs of three intermetallic phases, Au_3Cu (in the $L1_2$ structure), AuCu ($L1_0$), and $AuCu_3$ ($L1_2$), all three of which have been reported experimentally in the phase diagram of Au–Cu.[36] Comparing the random alloy DFs at the concentrations corresponding to these phases, one observes that the overall shape of the DFs is rather similar for ordered (intermetallic phase) and random alloys (Figure S6a–c, Supporting Information). In all cases there is a broad feature between approximately 2 and 6 eV, the position of which is dictated by the onset of the d-band (see below). There are, however, subtle differences in the fine structure. The ordered structures exhibit a pronounced feature around 3 eV that is absent in the DFs of the corresponding random alloys calculated for the same concentrations. The latter exhibit a much broader band with more dipole strength between 4 and 5 eV than their ordered intermetallic phase counter parts as a result of broken symmetry. In Au–Cu, composition thus has an even weaker impact on the DFs than ordering at the atomic level. The weak dependency of the DF on chemical ordering in Au–Cu was observed experimentally also by De Silva et al.[41] at 50% composition. We also note that our calculations agree with

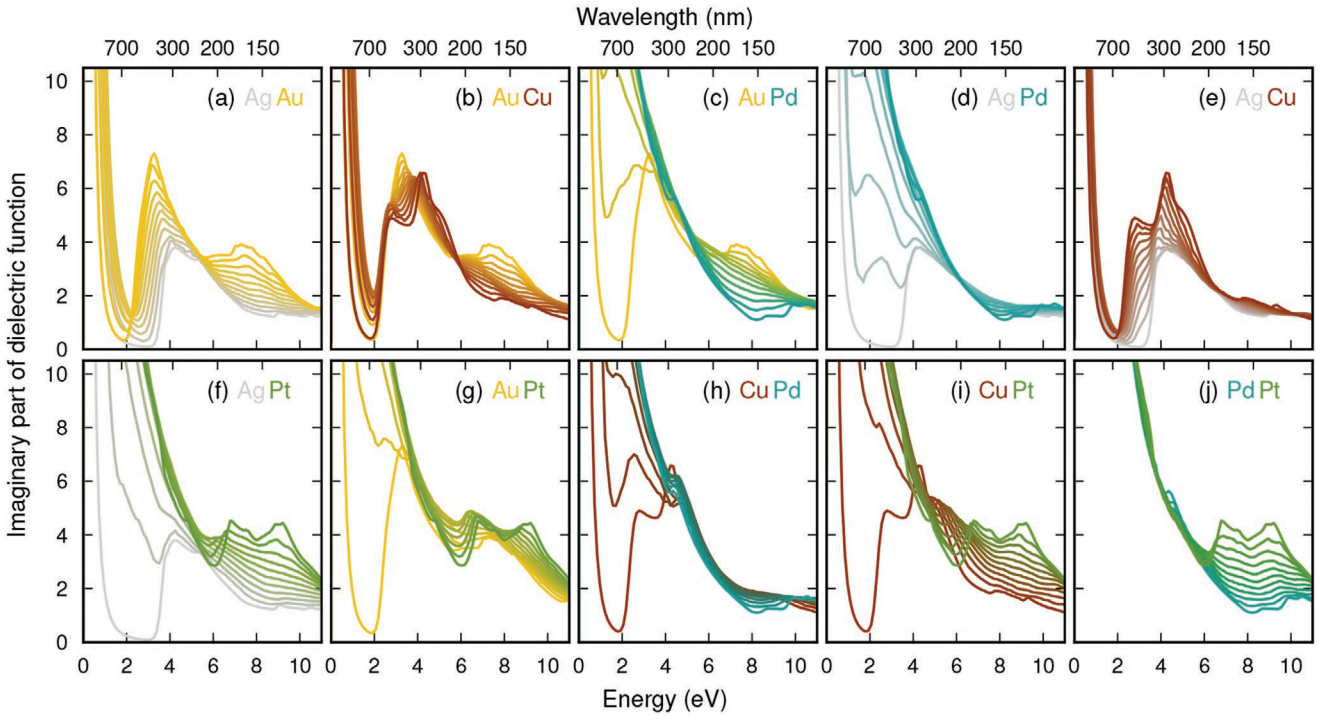

Figure 3. Library of calculated dielectric functions for the ten alloys formed by Ag, Au, Cu, Pd, and Pt, using special quasi-random structures at every 10 at% concentration between the pure phases. Alloys containing elements from both group 10 (here Pd or Pt) and group 11 (Cu, Ag, Au) are characterized by a rapid increase in the dielectric function at low photon energies when Cu, Ag, or Au is added to Pd or Pt, caused by transitions from the d-band to the states near the Fermi level. In contrast, alloys in which both elements are from the same group, exhibit an almost linear concentration dependence at all photon energies. See Figure S4, Supporting Information, for the real parts of the DFs.

some previous experimental studies with respect to the appearance of fine structures in the imaginary part of the DF for the ordered phases.[17,42,43]

It is now interesting to investigate the difference between random alloy and intermetallic phases in the optical response of the nanodisk system. We notice that the optical extinction spectra calculated using our DFs for random alloys agree well with the experimental results across the entire range of compositions (Figure 4b). Second, we find that the small differences in the DFs between ordered intermetallic phases and random alloy (SQS) translate to almost identical peak positions and FWHMs in the FDTD simulations (crosses in Figure 4b). This is true also if we consider *all* symmetrically distinct equiatomic (50%) orderings with up to 4 atoms in the primitive cell (Figure S7, Supporting Information, structures are provided in the Supporting Information). We thus conclude that for Au–Cu, the variation in DF with chemical order on the atomic scale is too small to be reliably resolved in the optical extinction spectra of single nanodisks calculated by FDTD. As will be shown below, the lack of sensitivity to order is, however, not generalizable.

Next, we consider the **Au–Pd** system that, unlike Ag–Au and Au–Cu, is *non-isovalent*, that is, Au has 10 d electrons and 1 s electron in its outermost electronic shells, whereas Pd has 10 d electrons only. In this case, we find that the composition dependence of random structures (SQS)-DFs is strongly nonlinear, in particular at energies below roughly 4 eV (Figure 3c; Figure S5c, Supporting Information), which is consistent with previous experimental studies (Figure S10, Supporting Information). This non-linearity translates to a non-linear and non-trivial composition dependence of peak position and FWHM in the optical extinction spectra of nanodisks in the corresponding FDTD simulations, which in turn are in very good agreement with the experiment (Figure 4c).

Au–Pd is thus qualitatively different from Au–Cu. Therefore, it is interesting to investigate the impact of atomic-scale ordering on DF and optical extinction spectra even though Au–Pd is in the experiment expected to form a random alloy in the full composition range at moderate temperatures.[36] Accordingly, we calculated the DFs of all atomic structures that can be created with 4 atoms or less in the primitive cell at a composition of 50% and the corresponding FDTD extinction spectra (Figure S7, Supporting Information). Strikingly, compared to Au–Cu, variations in peak position with composition are substantially larger and comparable to the variation over the full composition range. This indicates that chemical ordering in alloys cannot always be ignored when discussing the optical response of alloys. In fact, we propose that this dependency of the DF, and accordingly extinction spectra of nanodisks, on chemical order constitutes yet another handle for optimizing nanophotonic devices for specific purposes. Conversely, it should be possible to use in situ measured optical extinction spectra of alloy nanoparticles as a probe of chemical order in some systems, for example during annealing experiments. For these purposes, however, it is crucial that reference data of the type presented here are available for DFs of alloys with both well-defined atomic order and disorder.

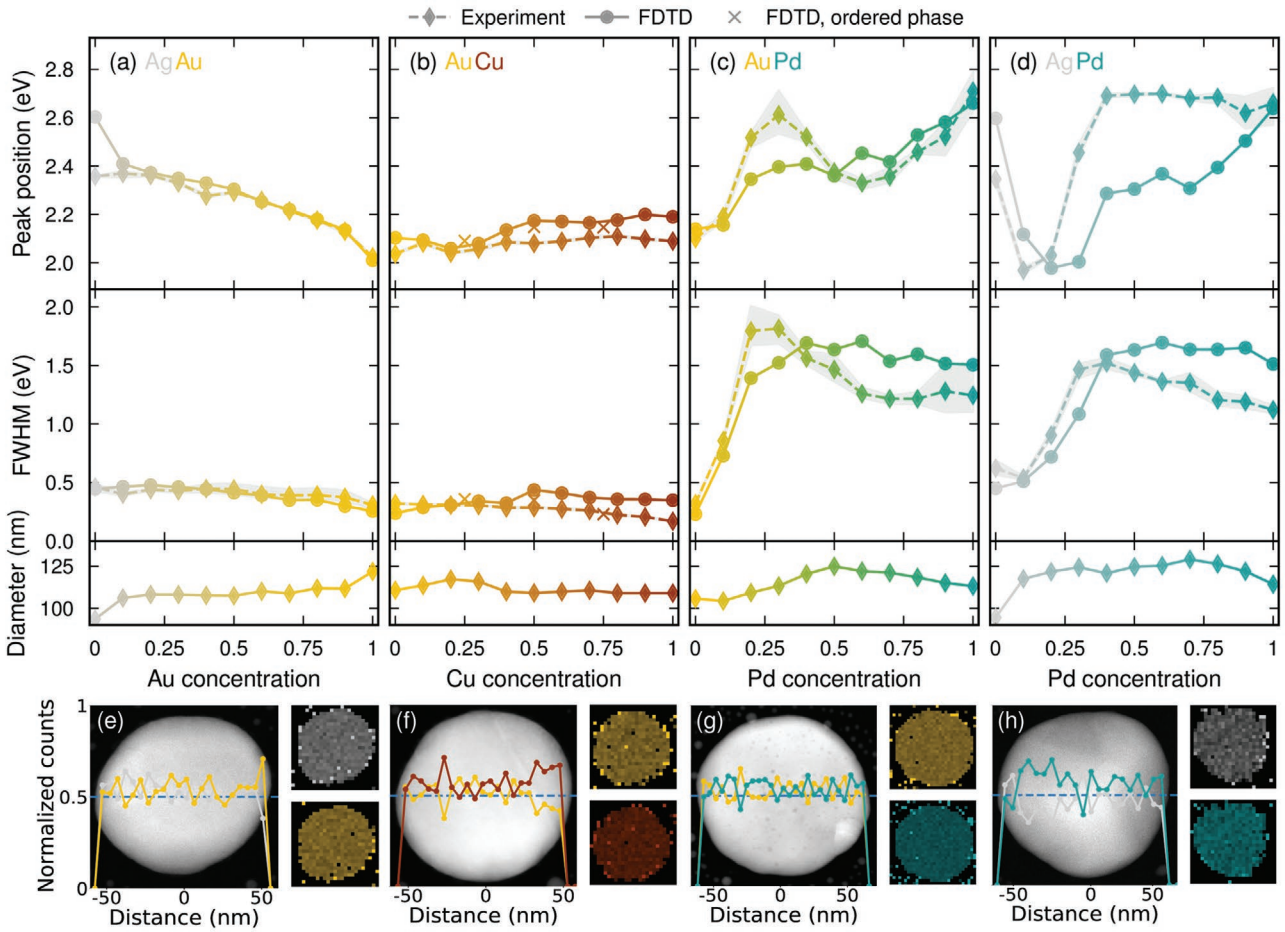

Figure 4. Peak position (upper row) and full width at half maximum (second row) extracted from the optical extinction spectra of a) Ag–Au, b) Au–Pd, c) Au–Cu, and d) Ag–Pd nanodisks as obtained with FDTD for a single particle using the dielectric functions computed in this work (solid lines, circles) and measured experimentally for quasi-random nanodisk arrays (dashed lines, diamonds). The grey areas indicate the spread in measured values at different positions on a sample. The result of ordered intermetallic phases translates to almost identical peak positions for Au–Cu (crosses in (b)). The average diameter of the nanodisks in the arrays (third row) used for the experiments was extracted from SEM images for each sample, and then used as input to describe the corresponding nanodisk in the FDTD simulations. HAADF-STEM image together with and elemental linescan and an elemental map obtained by STEM-EDS for a nominally 50:50 e) Ag–Au, f) Au–Pd, g) Au–Cu, and h) Ag–Pd nanodisk confirming the homogeneous distribution of the alloyants across the particle.

As the last example, we consider another non-isovalent system, **Ag–Pd**. Just as for Au–Pd, the composition dependence of the Ag–Pd DF is decidedly non-linear (Figure 3d; Figure S5d, Supporting Information), in good agreement with previous work (Figure S11, Supporting Information). The variation of peak position and FWHM with composition is in reasonable agreement between FDTD simulations and experiment, although FDTD predicts a slightly different peak position, in particularly close to 50%.

2.3. Impact of Electronic Structure

The qualitative differences between the DFs of isovalent (Ag–Au, Au–Cu) and non-isovalent (Au–Pd, Ag–Pd) systems can be traced to the electronic structure of the elements.[44,45] Ag and Au are noble metals with a full d-band that is located several eV below the Fermi level (**Figure 5**a). As a result, these two metals exhibit very clear and strong plasmon peaks. When mixing Ag and Au the basic character of the electronic states remains largely intact: states in the vicinity of the Fermi level have s-p character regardless of composition, while the d-band remains deep. This continuity translates into an almost linear shift of the d-band edge with composition (Figure 5c).

Pd, in contrast, has an incompletely filled d-band that intersects the Fermi level (Figure 5b). Alloying between Au and Pd therefore implies a change in the character of states between Fermi level and d-band. Therefore, already rather small amounts of Pd in Au are sufficient to induce a pronounced increase in the DOS between Fermi level and the Au d-band edge (Figure 5b), which gives rise to a non-linear shift of the alloy d-band with composition (Figure 5c). Translated to the nanodisk system at hand in our experiments, the localized surface plasmon resonance arises by resonant coupling of single-particle excitations close to the Fermi level, which are screened by virtual d-band transitions.[46] In Mie theory in the quasi-static

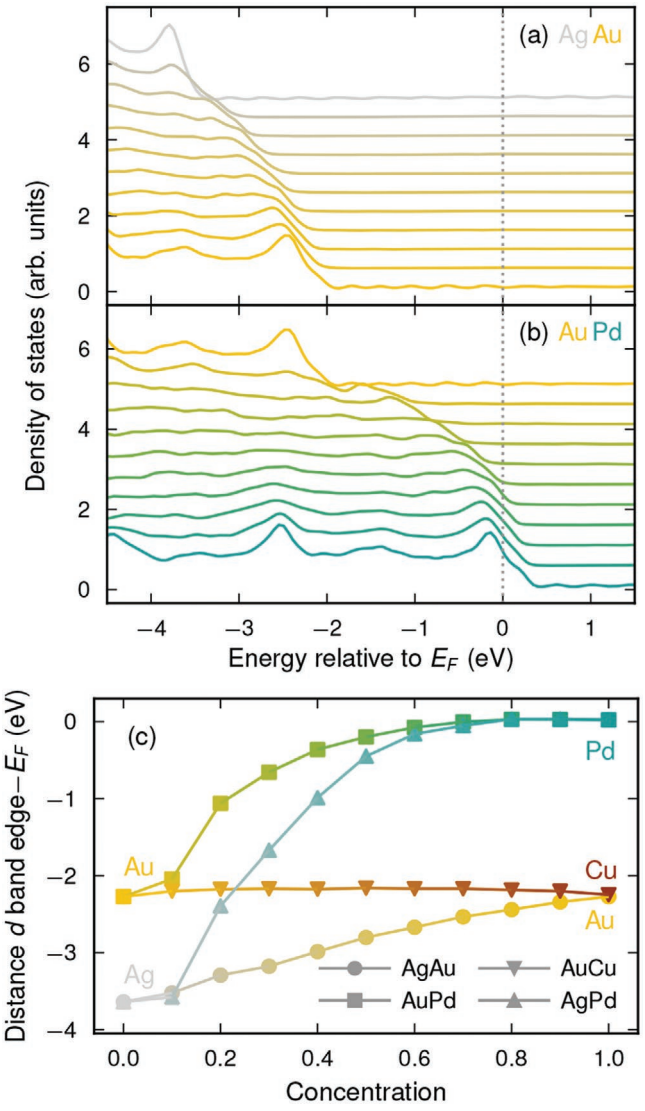

Figure 5. Density of states (DOS) for a) Ag–Au and b) Au–Pd at 11 equally spaced concentrations between 0% and 100%. Important for dielectric functions is the distance between the d-band edge and the Fermi level E_F (dotted line in (a)–(b)). c) Distance from d-band edge to Fermi level for Ag–Au, Au–Pd, Au–Cu, and Ag–Pd, defined as the energy at which the DOS is half the maximum DOS in the d-band.

regime, this corresponds to the condition $\mathrm{Re}\varepsilon(\omega) = -2$, which is satisfied at different energies depending on the free-electron density and the position of the d-band. The variations in the Au–Pd DOS with composition are therefore translated to the DF and the plasmonic alloy nanoparticle optical signatures, such as peak position and FWHM. Therefore, they are responsible for the experimentally observed strongly non-linear dependence of plasmonic response on alloy composition.

2.4. A Library of Dielectric Functions

Having demonstrated the accuracy of our computational approach by benchmarking with detailed experiments and electrodynamic simulations of the plasmonic properties of nanodisk arrays, we now feel confident to provide computational predictions of complex DFs for a much wider range of alloys, which all are of potential interest for nanophotonic, plasmonic, as well as photocatalytic applications. We have thus further expanded our library of DFs by including Ag–Cu, Ag–Pt, Au–Pt, Cu–Pd, Cu–Pt, and Pd–Pt (Figure 3e–j), such that it encompasses all ten binary alloys formed by combinations of Ag, Au, Cu, Pd, and Pt. As for the selected systems discussed above, also here we carried out LR-TDDFT calculations at every 10 at% in the full concentration range between the pure elements, as well as 25, 33, 67, and 75%. In this dense set of calculations, we then fitted Redlich–Kister polynomials to the concentration at each available energy (see Section 4 for details), which allows us to provide the DFs as continuous functions of both photon energy and concentration.

As a key point, we also highlight that all ten alloy systems indeed adhere to the general principles for isovalent and non-isovalent systems outlined above; the isovalent systems (Ag–Au, Ag–Cu, Au–Cu) all exhibit a close to linear concentration dependence, whereas the non-isovalent systems (Ag–Pd, Ag–Pt, Au–Pd, Au–Pt, Cu–Pd, Cu–Pt) are all rather non-linear at low photon energies. In particular, the imaginary part of the DF in the low-energy region increases quickly as Ag, Au, or Cu are added to Pd or Pt as a result of the addition of transitions from the d-band to states close to the Fermi level. As a special case, Pd–Pt is an isovalent system in which both elements are in group 10 of the periodic table, and thus have d-bands intersecting the Fermi level. Consequently, the DF is almost independent of concentration in the low-energy region, while at higher energies, the concentration dependency is close to linear. Since all systems follow these general principles, we obtain a generic design rule that can be used to select alloy and composition for a specific application.

Further comparisons of these data with experimentally determined DFs from the literature, where available, are deferred to Figures S12 and S13, Supporting Information. In addition to the SQS data, we also provide the DFs for the nine arguably most well-established face-centered cubic (FCC) intermetallic phases in the alloys at hand: Au_3Cu (in the $L1_2$ structure), AuCu ($L1_0$), $AuCu_3$ ($L1_2$), Ag_3Pt ($L1_2$), AgPt ($L1_1$), $AgPt_3$ ($L1_2$), Cu_3Pd ($L1_2$), Cu_3Pt ($L1_2$), and CuPt ($L1_1$) (Figure S6, Supporting Information).

3. Conclusions

We have from first principles calculated DFs for the ten binary alloys formed by combinations of the most common metals used in plasmonics, Ag, Au, Cu, Pd, and Pt, and found excellent agreement between the experimentally measured optical response of nanofabricated nanodisk arrays of four selected alloy systems (Ag–Au, Au–Cu, Au–Pd, Ag–Pd), and corresponding electrodynamic simulations using the computed DFs as key input. Our data revealed that the variation of the DF with concentration is non-trivial, in particular for non-isovalent alloys such as the combinations of Pd or Pt with Ag, Au, or Cu, and at low photon energies (long wavelengths). We attribute these differences to the behavior of the d-band,

specifically how the distance between the edge of the d-band and the Fermi level varies with composition in the different systems. This showcases, and explains at the atomic level, the unique opportunities offered by alloying for non-trivial optical response optimization in plasmonic nanostructures and metamaterials that go beyond the traditional engineering of size, shape, and organization of nanostructures in arrays. As a second key aspect, we highlight that several of the ten alloys presented here exhibit phase diagrams that contain intermetallic phases[36] (Au–Cu, Ag–Pt, Cu–Pt, Cu–Pd). In this context, the computational framework employed here allows one to elucidate the effect of order on the DF. Corresponding FDTD simulations reveal that the impact of intermetallic phase formation on the plasmonic response of nanodisks can be both large and small, depending on the system. Therefore, we predict that in situ plasmonic sensing[47,48] for some systems could enable the tracking of the evolution of order in alloy nanoparticles during annealing. Looking forward, we also anticipate that the methodology used here in general, and the calculated library of DFs in particular, will find wide application in the in silico screening and optimization of nanophotonic devices and optical metamaterials, where alloying offers an additional and so far largely unexplored handle for tuning of optical response and function. Furthermore, by providing a library of DFs, we eliminate the need for laborious experimental efforts to derive alloy DFs by trial and error, as well as all the experimental uncertainties highlighted in the introduction. Therefore, we have made this library available also via a web application (https://sharc.materialsmodeling.org/alloy_dielectric_functions/). Finally, we emphasize that the methods used in this paper are by no means limited to the systems presented but constitute a general framework for predicting the optical response of essentially any metallic alloy.

4. Experimental Section

Computational Methods–Calculation of Dielectric Functions: The ionic positions and cell shapes were first relaxed with density-functional theory (DFT) in the projector augmented wave formalism as implemented in the Vienna ab initio simulation package (version 5.4.1, PAW 2015)[49,50] using the vdW-DF-cx exchange-correlation functional,[51] until residual forces were below 10 meV Å^{-1} and stresses below 1 kbar. In these calculations, the wave functions were expanded in a plane wave basis set with a cutoff of 400 eV for alloys involving Cu and 384 eV for all other cases. The Brillouin zone (BZ) was sampled with a Γ-centered grid with a *k*-point density corresponding to $19 \times 19 \times 19$ *k*-points in the primitive cell. Occupations were set using the first-order Methfessel–Paxton scheme with a smearing parameter of 0.1 eV.

DFs were calculated using LR-TDDFT[26] as implemented in the GPAW package[52,53] (version 19.8.1 with GLLB-sc patched for extended metallic systems). In short, the macroscopic DF was calculated in reciprocal space through the linear density–density response function. Wave functions were expanded in a plane-wave basis with a cutoff at 340 eV. The occupation numbers were smeared according to a Fermi–Dirac distribution with a width of 0.1 eV. For calculations on SQS cells, the BZ was sampled with a Γ-centered grid with a density corresponding to 61 *k*-points in each direction for the undecorated (monoelemental) primitive cell. The *k*-point density was increased in smaller cells to obtain DFs that vary smoothly with photon energy. For pure elements, 237 *k*-points were used in each direction of the primitive cell. For $L1_0$, $L1_1$, $L1_2$ (Figure S6, Supporting Information), and enumerated structures (Figure S7, Supporting Information), a *k*-point density corresponding to, respectively, 261, 161, 281, and 121 *k*-points in each direction of the undecorated primitive cell, was used. These densities were chosen to account for the number of symmetry operations available in these structures, and the lower density in enumerated structures was sufficient as these DFs are not part of the library but were only used in FDTD simulations to assess the impact of chemical ordering.

DFs were obtained in the optical limit by evaluation at $\mathbf{q} = \mathbf{0}$. As discrete *k*-point sampling precludes intraband transitions with $\mathbf{q} \to \mathbf{0}$ and $\omega \to 0$, an intraband term, $\omega_P^2/(\omega + i\eta)^2$, was added to the DFs, where ω_P is the calculated plasma frequency, using the broadening parameter $\eta = 0.01$ eV. The ground state wave functions were obtained with the GLLB-sc exchange-correlation functional,[35] and dynamic exchange-correlation effects were taken into account within the adiabatic local-density approximation (ALDA) approximation. In the optical limit, ALDA results approach the random phase approximation (RPA) results, where the latter neglects dynamic exchange-correlation.[26]

The DFs were calculated with enumerated structures with up to four atoms per primitive cell, as well as SQSs with 20–24 atoms (depending on target concentration).[32,54,55] The latter were generated with a simulated annealing approach minimizing the deviation from the random limit of the cluster correlation of pairs shorter than 3.25*a* and triplets shorter than 1.5*a* (*a* being the lattice parameter), and with additional weight assigned to the cluster correlation of short-ranged pairs, using the default parameters suggested in ref. [56].

To suppress remaining effects of chemical order in SQS cells and to obtain DFs that vary smoothly with concentration, fourth-order Redlich–Kister polynomials

$$\epsilon(c,E) = c(1-c)\sum_{p=0}^{4} L_p(E)(1-2c)^p \quad (1)$$

were fit to DFs at each photon energy *E*. The fourth-order polynomials were chosen to yield a smoothly varying function while still reproducing the available data points well. The Redlich–Kister form ensures that the fitted DFs are reproduced exactly for the pure elements ($c = 0$ and 1).

Computational Methods–FDTD Simulations: Lumerical's FDTD Solution version 8.21.1882 was used to calculate the optical extinction spectra of the alloy nanodisks. Light was introduced as a linearly polarized plane wave via a total-field/scattered-field source and the scattering and absorption spectra were collected in all directions by integrating the Poynting vector of the field. A single disk was placed on a SiO_2 substrate with the DF from Lumerical's material database. To reduce computational time by a factor of four, the advantage of the particle symmetry was taken and symmetric and anti-symmetric boundary conditions were used. The disk was modelled as a tapered cylinder with rounded edges (6 nm rounding). The relevant disk diameter for each alloy composition was derived from SEM images of the corresponding experimental samples, which consisted of a quasi-random array. At least 500 particles from vastly different sample locations were analyzed and averaged for each composition assuming a circular shape and then using ImageJ to derive the average disk diameter for each alloy composition. This composition-specific average diameter was then used to set up the corresponding FDTD simulation, as well as to derive the thickness of the disk based on the assumption of conservation of volume from the as-prepared to annealed particles.

Experimental Methods–Nanofabrication: Quasi-random arrays of alloy nanodisks were fabricated using hole-mask colloidal lithography[33] and the method reported by Nugroho et al.[3] on either fused silica (for optical transmittance measurements), oxidized silicon (for SEM imaging) or transmission electron microscopy (TEM) window (for STEM imaging and EDS mapping) substrates. The TEM windows were fabricated as described in ref. [57] and used to obtain EDS elemental maps of selected alloy compositions. For cleaning prior to nanofabrication, the silicon and fused silica substrates were sonicated for 1 min in isopropanol, followed by 1 min in acetone, and then blow-dried in a nitrogen gas stream. The TEM windows were cleaned using the same chemicals but without

sonication to ensure the integrity of the windows. To prepare the hole-mask, 140 nm sulfonate latex beads from molecular probes were used. The alloy constituents were evaporated subsequently to the required thickness for a certain target alloy composition at a rate of 1 $Å s^{-1}$ at 1.2×10^{-6} mbar chamber base pressure (Lesker PVD 225). After lift-off in acetone, the samples were annealed in a flow reactor for 24 h at 500° in $(4.00 \pm 0.12)\%$ H_2 in Ar carrier gas at a flow rate of 500 mL min^{-1} to induce alloy formation and prevent oxidation.

Experimental Methods–Scanning Electron Microscopy: A *Zeiss Supra 55* and *Supra 60* were used. All images were recorded using the in-lens systems, at an acceleration voltage of 5 kV, 10 kV, or 15 kV and at a working distance of maximum 5 mm.

Experimental Methods–Scanning Transmission Electron Microscopy: The elemental EDS mapping and STEM images were acquired with a *FEI Titan 80-300* equipped with an *INCA X-sight* detector (*Oxford Instruments*) and operated at 300 kV. The distance was 5 nm between each position for which the spectra were acquired. Each spectrum was acquired during 5 s and the sample holder was tilted about 20° toward the detector to increase X-ray signal. The acquired spectra were analysed using *FEI TIA* version 4.3, the background was corrected for and the peaks fitted standard-less. The acquired weight percent were converted to atomic concentrations.

Experimental Methods–Spectrophotometry: Optical extinction spectra of all alloy samples were obtained using a *Cary 5000* spectrophotometer using a step width of 1 nm and an averaging time of 0.1 s.

Experimental Methods–Atomic Force Microscopy: A *Dimension 3100 Scanning Probe Microscope* from *Bruker* was used to obtain AFM topography scans of the samples. NSG-10 silicon probes with a high reflectivity gold coating from *NT-MDT* were used in tapping mode to image an area of 2 µm × 2 µm with 7.8 nm in-plane and 30 pm out-of-plane resolution. The scan rate was 1 Hz and adjusted such that trace and back-trace match. To process the data *NanoScope 6.14R1* and *Gwyddion 2.51* softwares were used.

Experimental Methods–X-Ray Photoelectron Spectroscopy: XPS measurements were performed with a *PHI 5000* (*Physical Electronics*). The monochromatized K_α-line of aluminum with a energy of 1486.6 eV was used for photo excitation. For the overview spectra an energy step width of 0.125 eV and a pass energy of 58.70 eV was used. All spectra were corrected by setting the adventitious C-1s peak of the C–C bond to 284.8 eV.

Supporting Information

Supporting Information is available from the Wiley Online Library or from the author.

Acknowledgements

J.M.R. and C.T. contributed equally to this work. The work was funded by the Knut and Alice Wallenberg Foundation projects 2014.0226, 2016.0210, and 2015.0055, the Swedish Research Council project grants 2015-04153, 2015-05115, and 2018-06482, and the Swedish Foundation for Strategic Research Materials framework grant RMA15-0052. T.P.R. acknowledges support from the European Union's Horizon 2020 research and innovation programme under the Marie Skłodowska-Curie grant agreement No 838996. Part of this work was carried out at the MC2 cleanroom facility and at the Chalmers Materials Analysis Laboratory. Computer time allocations by the Swedish National Infrastructure for Computing at C3SE (Gothenburg), NSC (Linköping), and PDC (Stockholm) are gratefully acknowledged.

Conflict of Interest

The authors declare no conflict of interest.

Keywords

nanoalloys, nanofabrication, optical response, time-dependent density-functional theory

Received: March 6, 2020
Revised: May 12, 2020
Published online: June 1, 2020

[1] Z. W. Seh, J. Kibsgaard, C. F. Dickens, I. Chorkendorff, J. K. Nørskov, T. F. Jaramillo, *Science* **2017**, *355*, 4998.
[2] C. Wadell, F. A. A. Nugroho, E. Lidström, B. Iandolo, J. B. Wagner, C. Langhammer, *Nano Lett.* **2015**, *15*, 3563.
[3] F. A. A. Nugroho, B. Iandolo, J. B. Wagner, C. Langhammer, *ACS Nano* **2016**, *10*, 2871.
[4] P.-C. Chen, X. Liu, J. L. Hedrick, Z. Xie, S. Wang, Q.-Y. Lin, M. C. Hersam, V. P. Dravid, C. A. Mirkin, *Science* **2016**, *352*, 1565.
[5] M. R. S. Dias, M. S. Leite, *Acc. Chem. Res.* **2019**, *52*, 2881.
[6] C. Gong, M. R. S. Dias, G. C. Wessler, J. A. Taillon, L. G. Salamanca-Riba, M. S. Leite, *Adv. Opt. Mater.* **2017**, *5*, 1600568.
[7] C. Gong, A. Kaplan, Z. A. Benson, D. R. Baker, J. P. McClure, A. R. Rocha, M. S. Leite, *Adv. Opt. Mater.* **2018**, *6*, 1800218.
[8] Y. Hashimoto, G. Seniutinas, A. Balčytis, S. Juodkazis, Y. Nishijima, *Sci. Rep.* **2016**, *6*, 25010.
[9] S. Kadkhodazadeh, F. A. A. Nugroho, C. Langhammer, M. Beleggia, J. B. Wagner, *ACS Photonics* **2019**, *6*, 779.
[10] S. Thota, Y. Wang, J. Zhao, *Mater. Chem. Front.* **2018**, *2*, 1074.
[11] I. Darmadi, F. A. A. Nugroho, S. Kadkhodazadeh, J. B. Wagner, C. Langhammer, *ACS Sens.* **2019**, *4*, 1424.
[12] F. A. A. Nugroho, I. Darmadi, L. Cusinato, A. Susarrey-Arce, H. Schreuders, L. J. Bannenberg, A. B. d. S. Fanta, S. Kadkhodazadeh, J. B. Wagner, T. J. Antosiewicz, A. Hellman, V. P. Zhdanov, B. Dam, C. Langhammer, *Nat. Mater.* **2019**, *18*, 489.
[13] K. Sytwu, M. Vadai, J. A. Dionne, *Adv. Phys.: X* **2019**, *4*, 1619480.
[14] D. Rioux, S. Vallières, S. Besner, P. Muñoz, E. Mazur, M. Meunier, *Adv. Opt. Mater.* **2014**, *2*, 176.
[15] H. Fukutani, *J. Phys. Soc. Jpn.* **1971**, *30*, 399.
[16] C. Gong, M. S. Leite, *ACS Photonics* **2016**, *3*, 507.
[17] C. L. Foiles, *Landolt-Börnstein-Group III Condensed Matter 15B (Electrical Resistivity, Thermoelectrical Power and Optical Properties)* (Eds: K.-H. Hellwege, J. L. Olsen), Springer, Berlin **1985**.
[18] J. Rivory, *J. Phys. Colloq.* **1974**, *35*, C4.
[19] S. Molesky, Z. Lin, A. Y. Piggott, W. Jin, J. Vucković, A. W. Rodriguez, *Nat. Photonics* **2018**, *12*, 659.
[20] K. M. McPeak, S. V. Jayanti, S. J. P. Kress, S. Meyer, S. Iotti, A. Rossinelli, D. J. Norris, *ACS Photonics* **2015**, *2*, 326.
[21] D. I. Yakubovsky, A. V. Arsenin, Y. V. Stebunov, D. Y. Fedyanin, V. S. Volkov, *Opt. Express* **2017**, *25*, 25574.
[22] R. L. Olmon, B. Slovick, T. W. Johnson, D. Shelton, S.-H. Oh, G. D. Boreman, M. B. Raschke, *Phys. Rev. B* **2012**, *86*, 235147.
[23] O. Peña-Rodríguez, U. Pal, *J. Opt. Soc. Am. B* **2011**, *28*, 2735.
[24] A. Ciesielski, L. Skowronski, M. Trzcinski, E. Górecka, P. Trautman, T. Szoplik, *Surface Science* **2018**, *674*, 73.
[25] K. J. J. Mayrhofer, K. Hartl, V. Juhart, M. Arenz, *J. Am. Chem. Soc.* **2009**, *131*, 16348.
[26] C. A. Ullrich, *Time-Dependent Density-Functional Theory: Concepts and Applications*, Oxford University Press, Oxford **2012**.
[27] W. S. M. Werner, K. Glantschnig, C. Ambrosch-Draxl, *J. Phys. Chem. Ref. Data* **2009**, *38*, 1013.
[28] M. Stiehler, S. Kaltenborn, S. S. A. Gillani, P. Pudwell, H. C. Schneider, P. Häussler, *J. Electron Spectrosc. Relat. Phenom.* **2015**, *202*, 102.
[29] Z. Ning, C.-T. Liang, Y.-C. Chang, *Phys. Rev. B* **2017**, *96*, 085202.

[30] V. M. Silkin, R. D. Muiño, I. P. Chernov, E. V. Chulkov, P. M. Echenique, *J. Phys.: Condens. Matter* **2012**, *24*, 104021.
[31] M. A. Poyli, V. M. Silkin, I. P. Chernov, P. M. Echenique, R. D. Muiño, J. Aizpurua, *J. Phys. Chem. Lett.* **2012**, *3*, 2556.
[32] A. Zunger, S. H. Wei, L. G. Ferreira, J. E. Bernard, *Phys. Rev. Lett.* **1990**, *65*, 353.
[33] H. Fredriksson, Y. Alaverdyan, A. Dmitriev, C. Langhammer, D. S. Sutherland, M. Zäch, B. Kasemo, *Adv. Mater.* **2007**, *19*, 4297.
[34] O. Gritsenko, R. van Leeuwen, E. van Lenthe, E. J. Baerends, *Phys. Rev. A* **1995**, *51*, 1944.
[35] M. Kuisma, J. Ojanen, J. Enkovaara, T. T. Rantala, *Phys. Rev. B* **2010**, *82*, 115106.
[36] T. Massalski, editor, *Binary Alloy Phase Diagram*, ASM International, Materials Park, OH **1990**.
[37] O. Peña-Rodríguez, M. Caro, A. Rivera, J. Olivares, J. M. Perlado, A. Caro, *Opt. Mater. Express* **2014**, *4*, 403.
[38] S. Link, Z. L. Wang, M. A. El-Sayed, *J. Phys. Chem. B* **1999**, *103*, 3529.
[39] Y. Nishijima, S. Akiyama, *Opt. Mater. Express* **2012**, *2*, 1226.
[40] The discrepancy in peak position in pure Ag may stem from uncertainties in geometry and/or oxidation during ageing; see also Figures S16 and S17, Supporting Information.
[41] K. S. B. D. Silva, A. Gentle, M. Arnold, V. J. Keast, M. B. Cortie, *J. Phys. D: Appl. Phys.* **2015**, *48*, 215304.
[42] W. R. Scott, L. Muldawer, *Phys. Rev. B* **1976**, *14*, 4426.
[43] J. Rivory, *Phys. Rev. B* **1977**, *15*, 3119.
[44] C. Kittel, *Introduction to Solid State Physics*, 8th ed., John Wiley & Sons, New York **2005**.
[45] T. Gong, J. N. Munday, *Opt. Mater. Express* **2015**, *5*, 2501.
[46] T. P. Rossi, M. Kuisma, M. J. Puska, R. M. Nieminen, P. Erhart, *J. Chem. Theory Comput.* **2017**, *13*, 4779.
[47] M. Schwind, V. P. Zhdanov, I. Zorić, B. Kasemo, *Nano Lett.* **2010**, *10*, 931.
[48] C. Langhammer, E. M. Larsson, B. Kasemo, I. Zorić, *Nano Lett.* **2010**, *10*, 3529.
[49] G. Kresse, J. Furthmüller, *Comput. Mater. Sci.* **1996**, *6*, 15.
[50] G. Kresse, D. Joubert, *Phys. Rev. B* **1999**, *59*, 1758.
[51] K. Berland, P. Hyldgaard, *Phys. Rev. B* **2014**, *89*, 035412.
[52] J. Enkovaara, C. Rostgaard, J. J. Mortensen, J. Chen, M. Dułak, L. Ferrighi, J. Gavnholt, C. Glinsvad, V. Haikola, H. A. Hansen, H. H. Kristoffersen, M. Kuisma, A. H. Larsen, L. Lehtovaara, M. Ljungberg, O. Lopez-Acevedo, P. G. Moses, J. Ojanen, T. Olsen, V. Petzold, N. A. Romero, J. Stausholm-Møller, M. Strange, G. A. Tritsaris, M. Vanin, M. Walter, B. Hammer, H. Häkkinen, G. K. H. Madsen, R. M. Nieminen, J. K. Nørskov, M. Puska, T. T. Rantala, J. Schiøtz, K. S. Thygesen, K. W. Jacobsen, *J. Phys.: Condens. Matter* **2010**, *22*, 253202.
[53] J. Yan, J. J. Mortensen, K. W. Jacobsen, K. S. Thygesen, *Phys. Rev. B* **2011**, *83*, 245122.
[54] M. Ångqvist, W. A. Muñoz, J. M. Rahm, E. Fransson, C. Durniak, P. Rozyczko, T. H. Rod, P. Erhart, *Adv. Theory Simul.* **2019**, *2*, 1900015.
[55] A. Larsen, J. Mortensen, J. Blomqvist, I. Castelli, R. Christensen, M. Dulak, J. Friis, M. Groves, B. Hammer, C. Hargus, E. Hermes, P. Jennings, P. Jensen, J. Kermode, J. Kitchin, E. Kolsbjerg, J. Kubal, K. Kaasbjerg, S. Lysgaard, J. Maronsson, T. Maxson, T. Olsen, L. Pastewka, A. Peterson, C. Rostgaard, J. Schiøtz, O. Schütt, M. Strange, K. Thygesen, T. Vegge, L. Vilhelmsen, M. Walter, Z. Zeng, K. W. Jacobsen, *J. Phys.: Condens. Matter* **2017**, *29*, 273002.
[56] A. Van De Walle, P. Tiwary, M. De Jong, D. L. Olmsted, M. Asta, A. Dick, D. Shin, Y. Wang, L. Q. Chen, Z. K. Liu, *Comput. Coupling Phase Diagrams Thermochem.* **2013**, *42*, 13.
[57] A. W. Grant, Q.-H. Hu, B. Kasemo, *Nanotechnology* **2004**, *15*, 1175.

ADVANCED FUNCTIONAL MATERIALS

Supporting Information

for *Adv. Funct. Mater.*, DOI: 10.1002/adfm.202002122

A Library of Late Transition Metal Alloy Dielectric Functions for Nanophotonic Applications

*J. Magnus Rahm, Christopher Tiburski, Tuomas P. Rossi, Ferry Anggoro Ardy Nugroho, Sara Nilsson, Christoph Langhammer, and Paul Erhart**

Supporting Information

A Library of Late Transition Metal Alloy Dielectric Functions for Nanophotonic Applications

J. Magnus Rahm, Christopher Tiburski, Tuomas P. Rossi,
Ferry Anggoro Ardy Nugroho, Sara Nilsson, Christoph Langhammer, and Paul Erhart

Contents

Figures

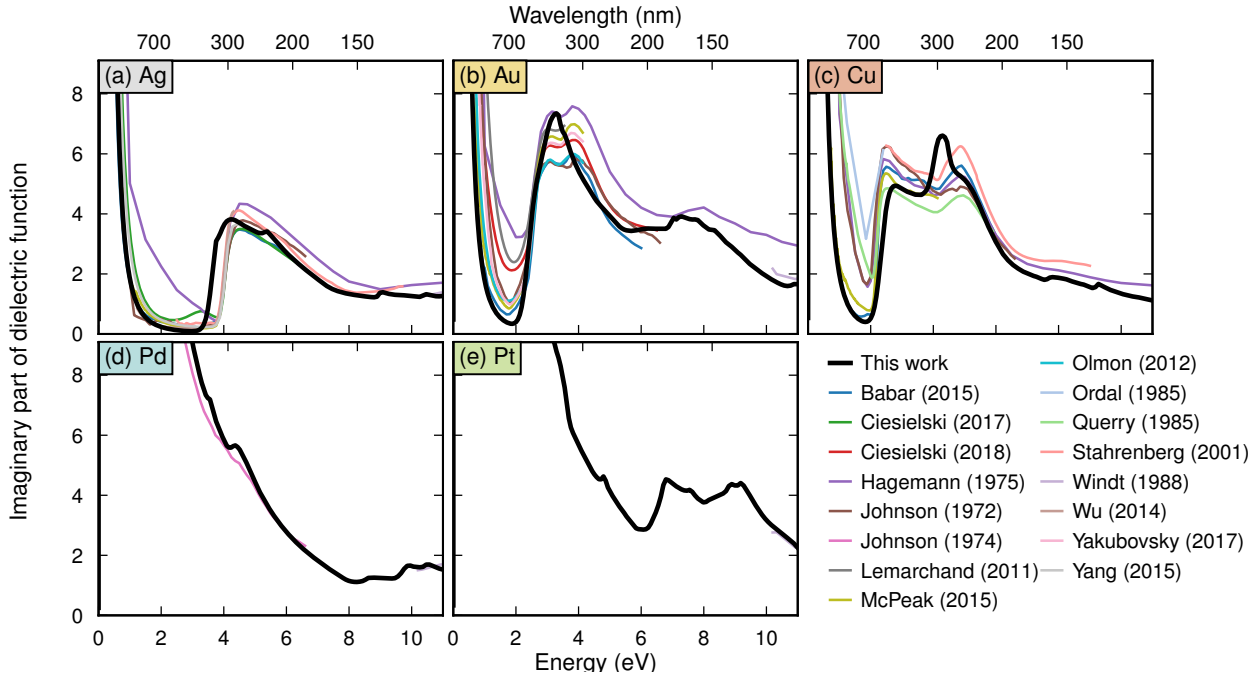

Figure S1: Imaginary part of dielectric functions of pure elements. Calculated imaginary parts of dielectric functions for pure elements (thick black lines) compared to experimental data (1–17) (thin colored lines). Experimental data exhibit large variations but we note a few systematic disagreements with our results: the energy at which the DF rises due to onset of transitions from the d-band is underestimated for Ag and overestimated in Cu. Experimental DFs for Au, generally exhibit a double peak structure between 2 and 4 eV, whereas our calculation shows a single peak, which we attribute to the neglect of spin-orbit coupling.

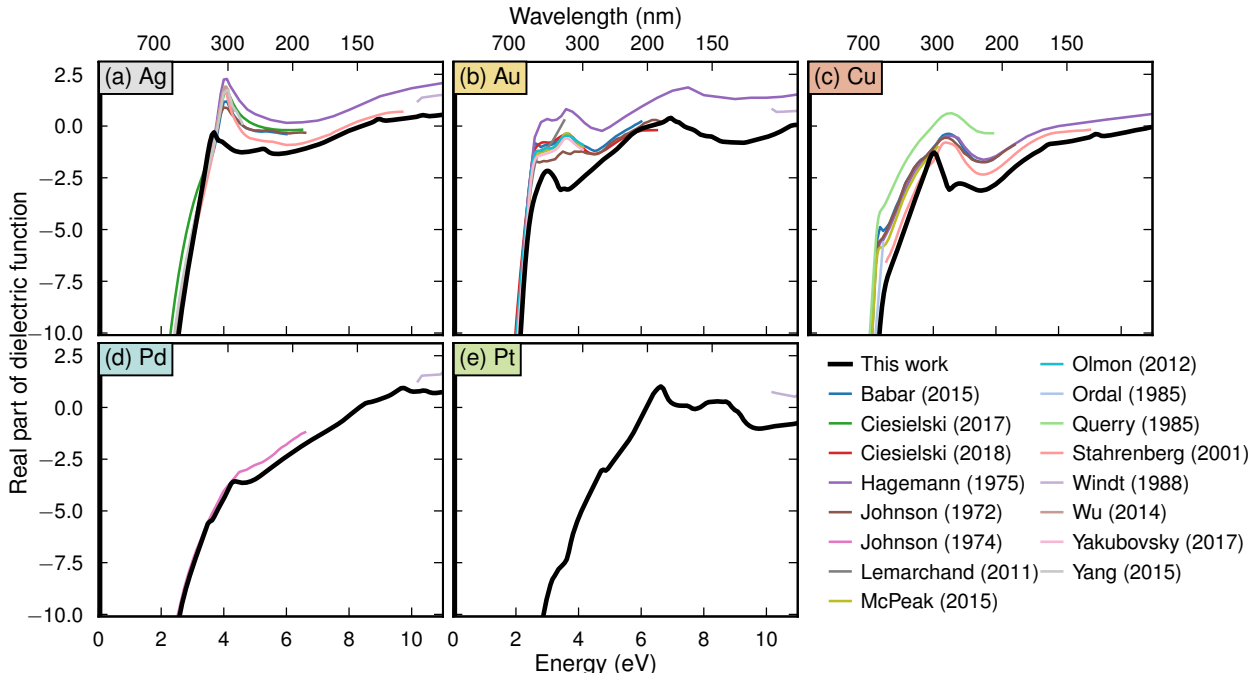

Figure S2: Real part of dielectric functions of pure elements. Calculated real parts of dielectric functions for pure elements (thick black lines) compared to experimental data (1–17) (thin colored lines).

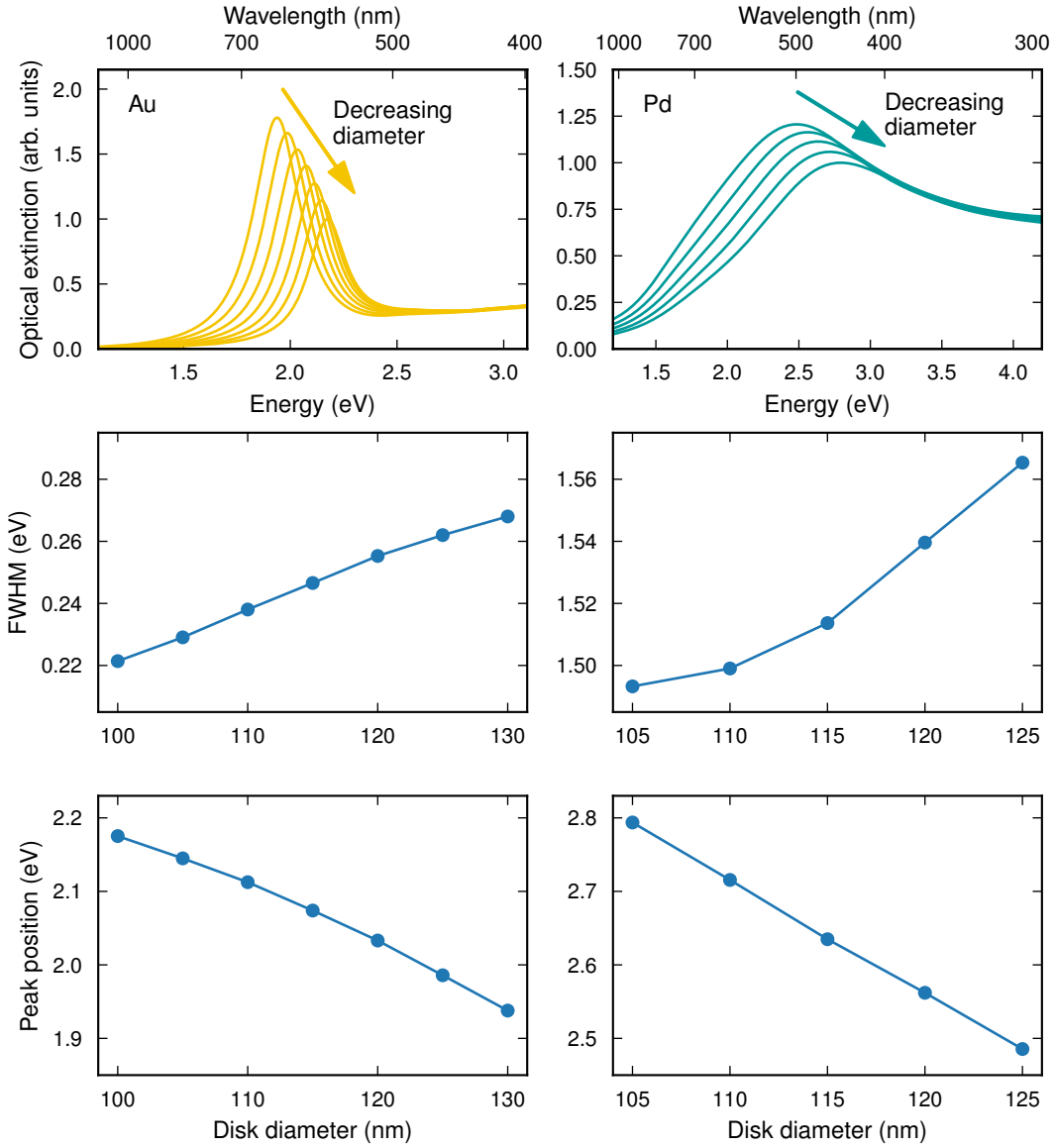

Figure S3: Impact of diameter of nanodisks on their optical extinction spectra. Optical extinction spectra obtained by FDTD simulations (top) of nanodisks of Au (left) and Pd (right) together with corresponding FWHM (middle row) and peak position (bottom row).

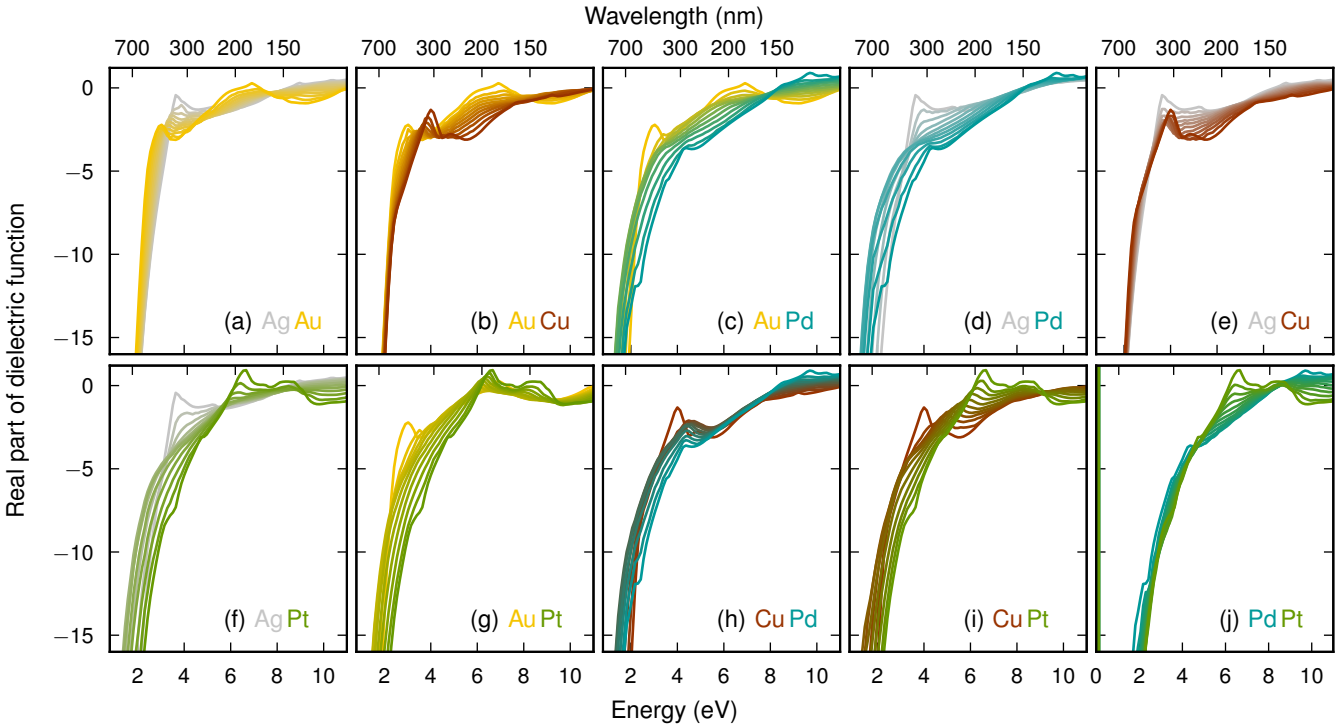

Figure S4: Real part of dielectric functions of alloys. Real part of calculated dielectric functions for the ten alloys formed by Ag, Au, Cu, Pd, and Pt at every 10% concentration between the pure phases.

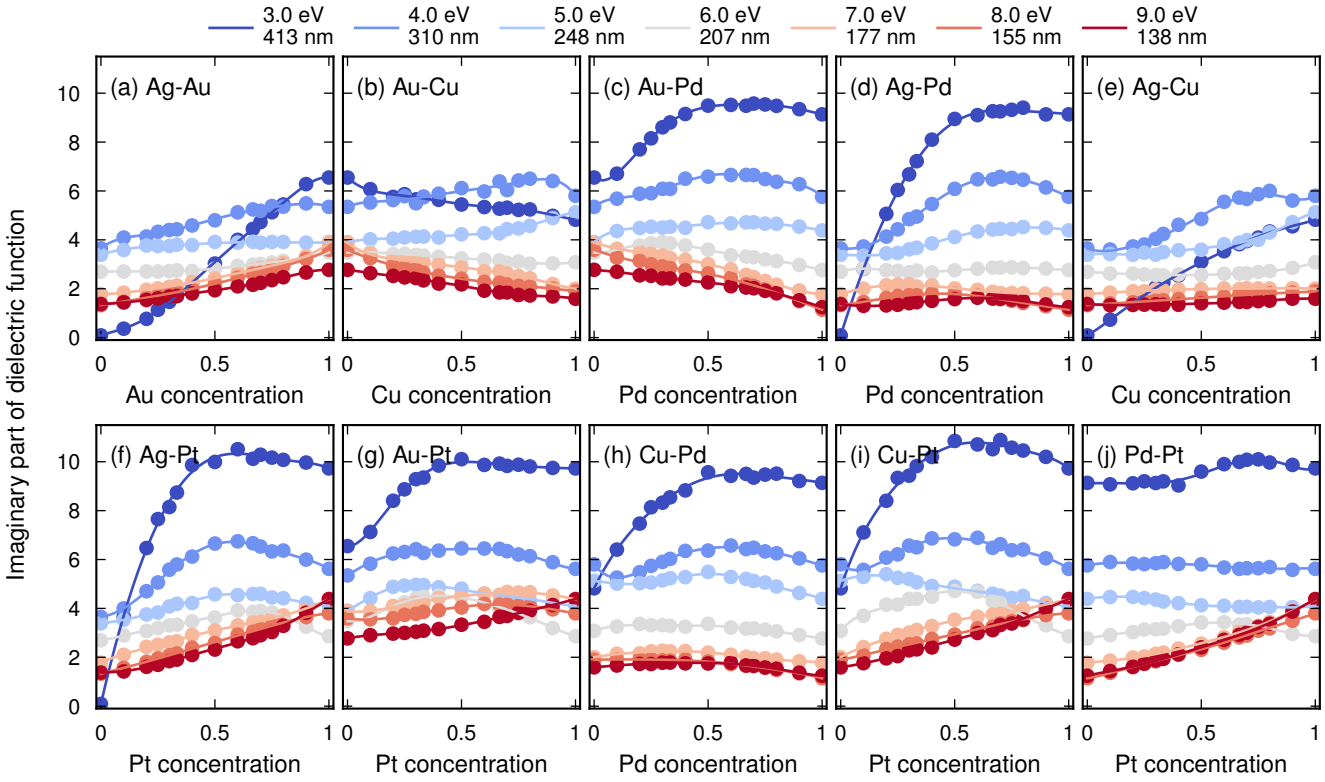

Figure S5: Concentration dependence of dielectric functions of alloys. Calculated dielectric functions for the ten alloys formed by Ag, Au, Cu, Pd, and Pt as a function of concentration at discrete values of energy. Dots indicate calculated values, lines are fits to Redlich–Kister polynomials.

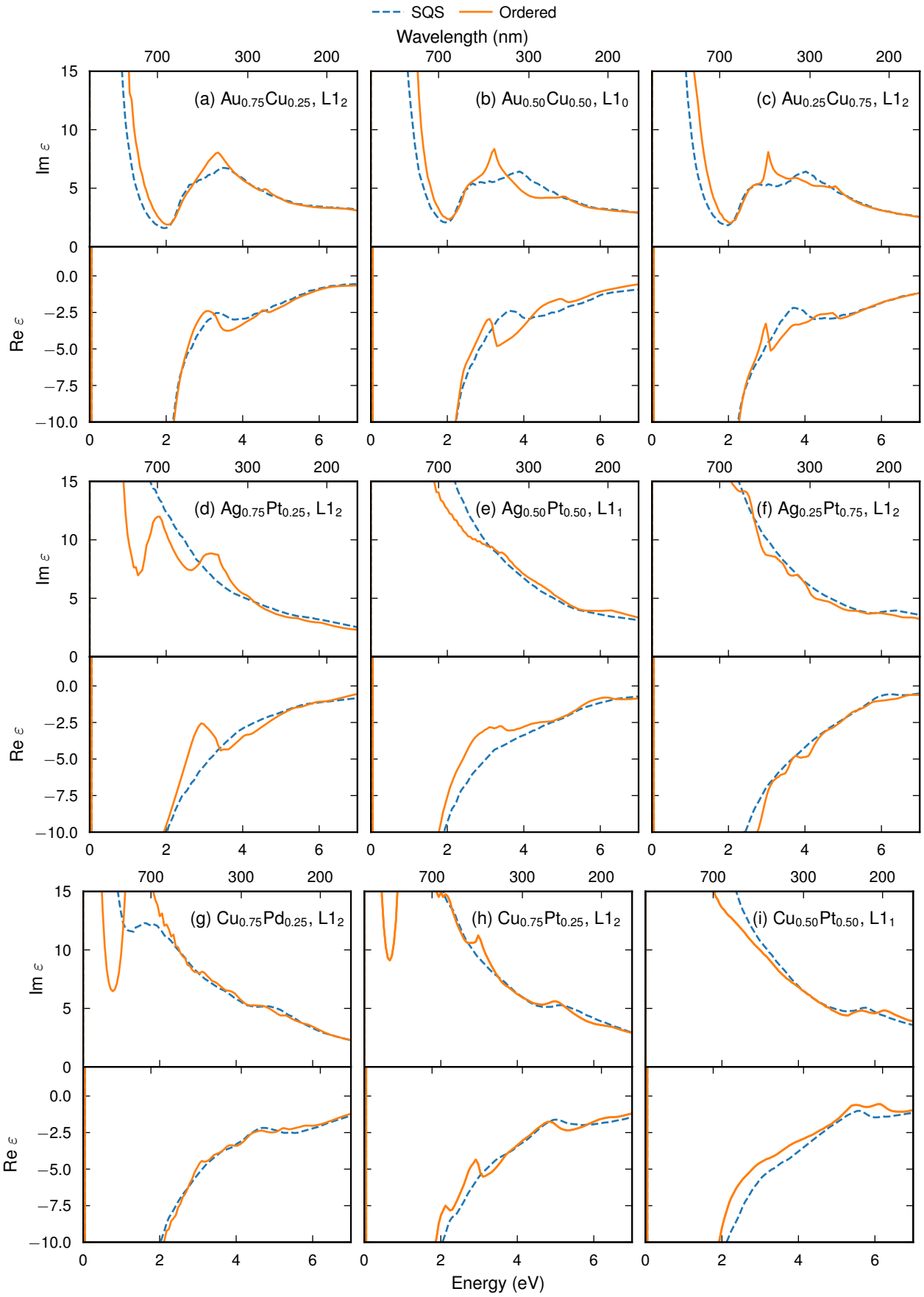

Figure S6: Dielectric functions of intermetallic phases. Calculated dielectric functions for intermetallic phases (full, orange lines) and SQS cells of the same composition (dashed, blue lines), for (a) $Au_{0.75}Cu_{0.25}$ (intermetallic phase: $L1_2$), (b) $Au_{0.5}Cu_{0.5}$ ($L1_0$), (c) $Au_{0.25}Cu_{0.75}$ ($L1_2$), (d) $Ag_{0.75}Pt_{0.25}$ ($L1_2$), (e) $Ag_{0.5}Pt_{0.5}$ ($L1_1$), (f) $Ag_{0.25}Pt_{0.75}$ ($L1_2$), (g) $Cu_{0.75}Pd_{0.25}$ ($L1_2$), (h) $Cu_{0.75}Pt_{0.25}$ ($L1_2$), and (i) $Cu_{0.5}Pt_{0.5}$ ($L1_1$).

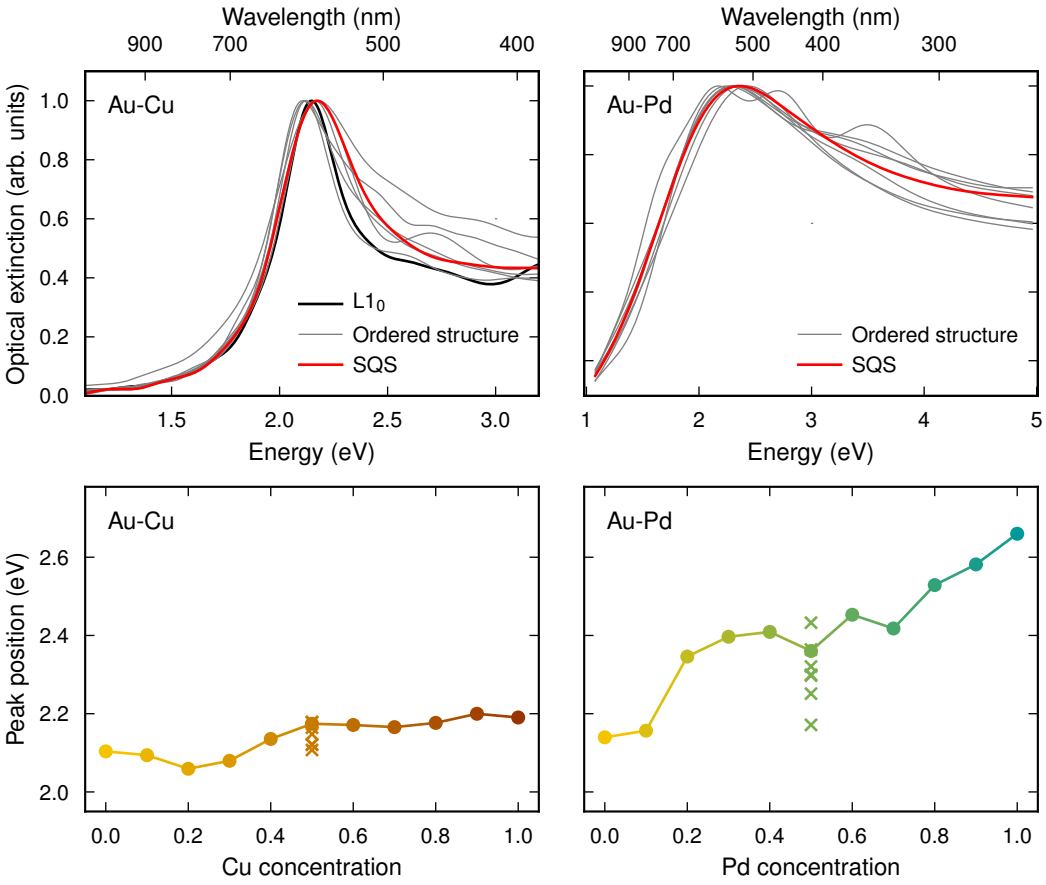

Figure S7: Impact of chemical order on the optical extinction spectra of $Au_{0.5}Cu_{0.5}$ and $Au_{0.5}Pd_{0.5}$ alloys. Optical extinction spectra (top row) for $Au_{0.5}Cu_{0.5}$ (left) and $Au_{0.5}Pd_{0.5}$ (right), using SQS (red lines) as well as all structures with four atoms or less in the unit cell. The AuCu intermetallic $L1_0$ is highlighted in solid black. The corresponding peak positions (bottom row, crosses) in comparison with the spread of peak position of SQS over the full concentration range (dots).

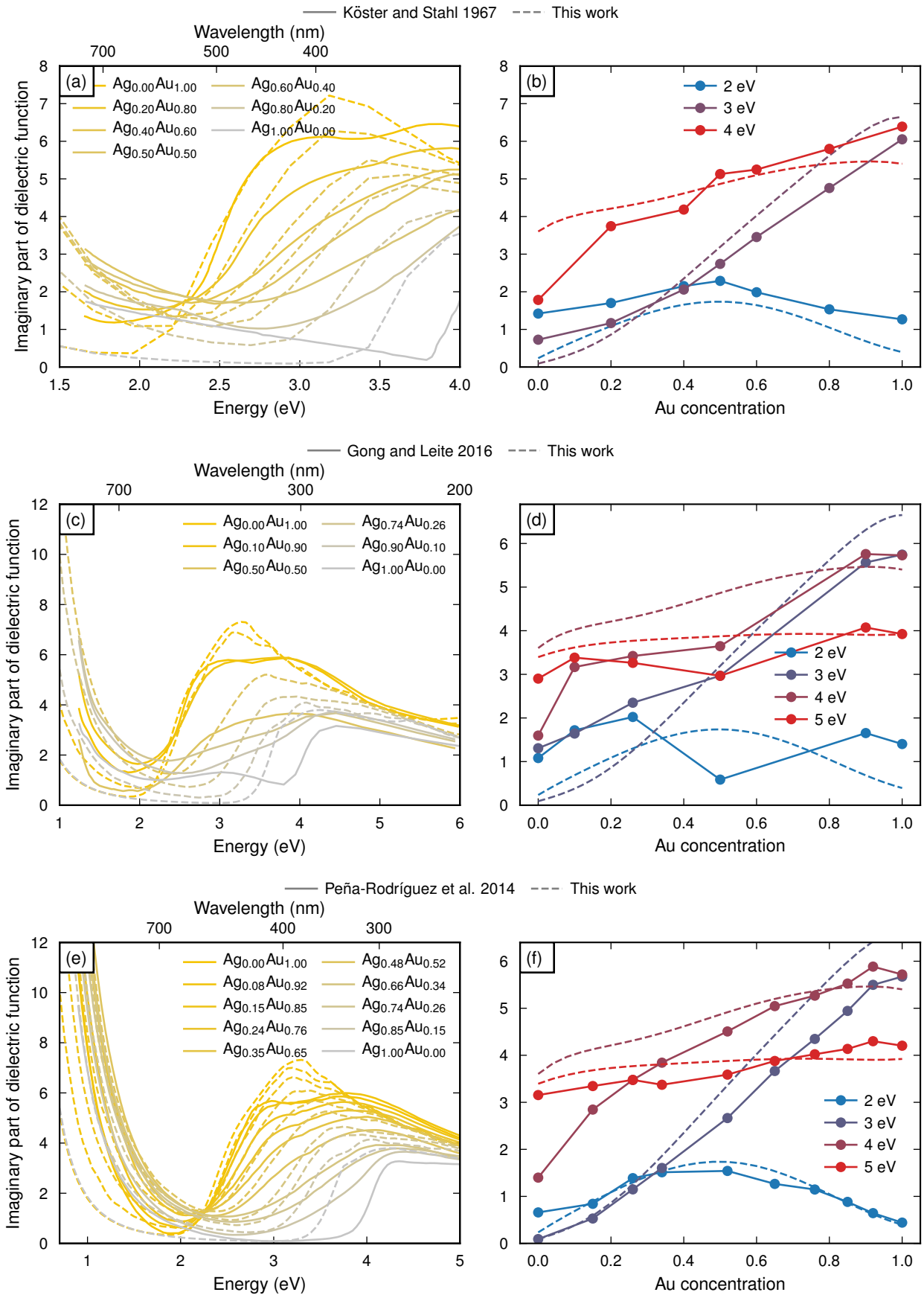

Figure S8: Comparison of Ag–Au alloy dielectric functions to experimental data. Dielectric function of Ag–Au, comparing our calculated DFs (dashed lines) to those of (18) (a–b), (19) (c–d), and (20) (e–f) as a function of photon energy (left) for all the concentrations presented in the respective references, and concentration (right) at specific photon energies.

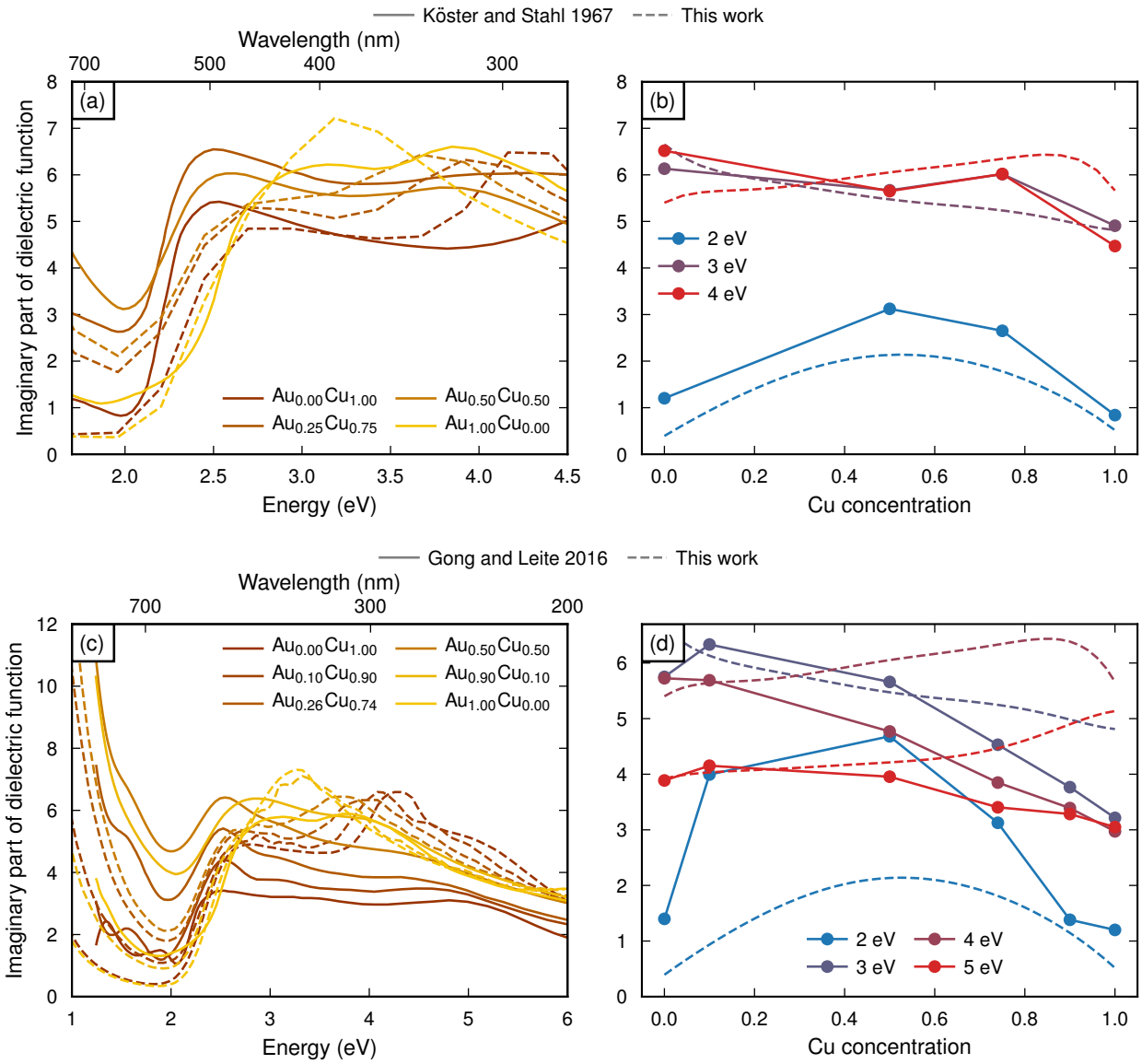

Figure S9: Comparison of Au–Cu alloy dielectric functions to experimental data. Dielectric function of Au–Cu, comparing our calculated DFs (dashed lines) to those of (18) (a–b) and (19) (c–d) as a function of photon energy (left) for all the concentrations presented in the respective references, and concentration (right) at specific photon energies.

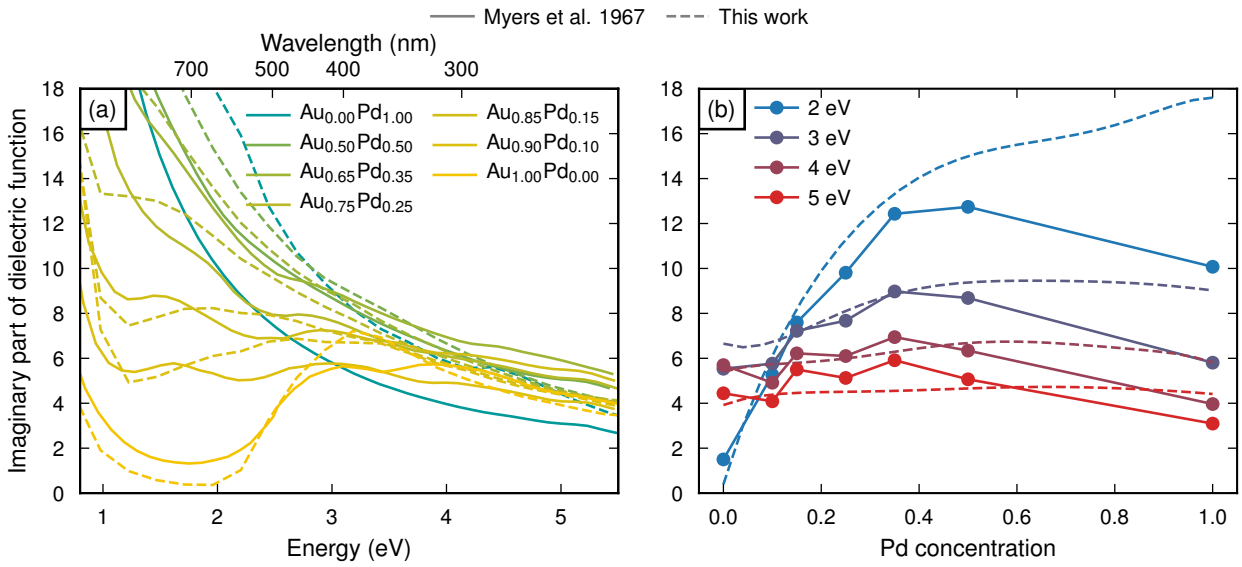

Figure S10: Comparison of Au–Pd alloy dielectric functions to experimental data. Dielectric function of Au–Pd, comparing our calculated DFs (dashed lines) to those of Ref. 21 (full lines, as reproduced in Ref. 22) as a function of (a) photon energy, for all the concentrations presented in Ref. 22, and (b) concentration at specific photon energies.

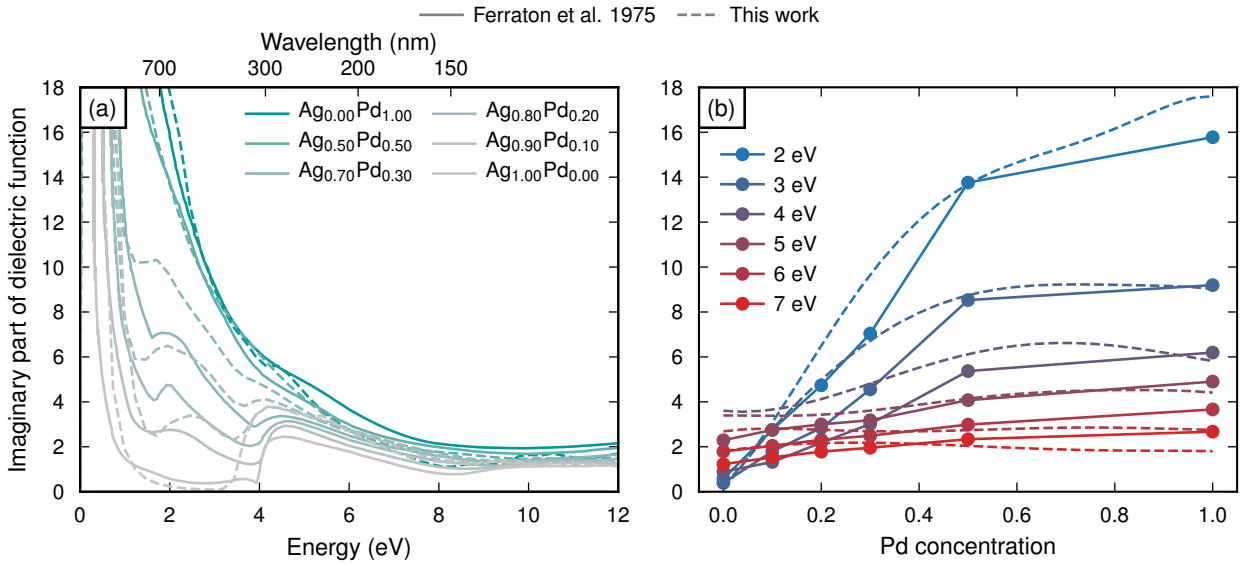

Figure S11: Comparison of Ag–Pd alloy dielectric functions to experimental data. Dielectric function of Ag–Pd, comparing our calculated DFs (dashed lines) to those of Ref. 23 (full lines, as reproduced in Ref. 22) as a function of (a) photon energy, for all the concentrations presented in Ref. 22, and (b) concentration at specific photon energies.

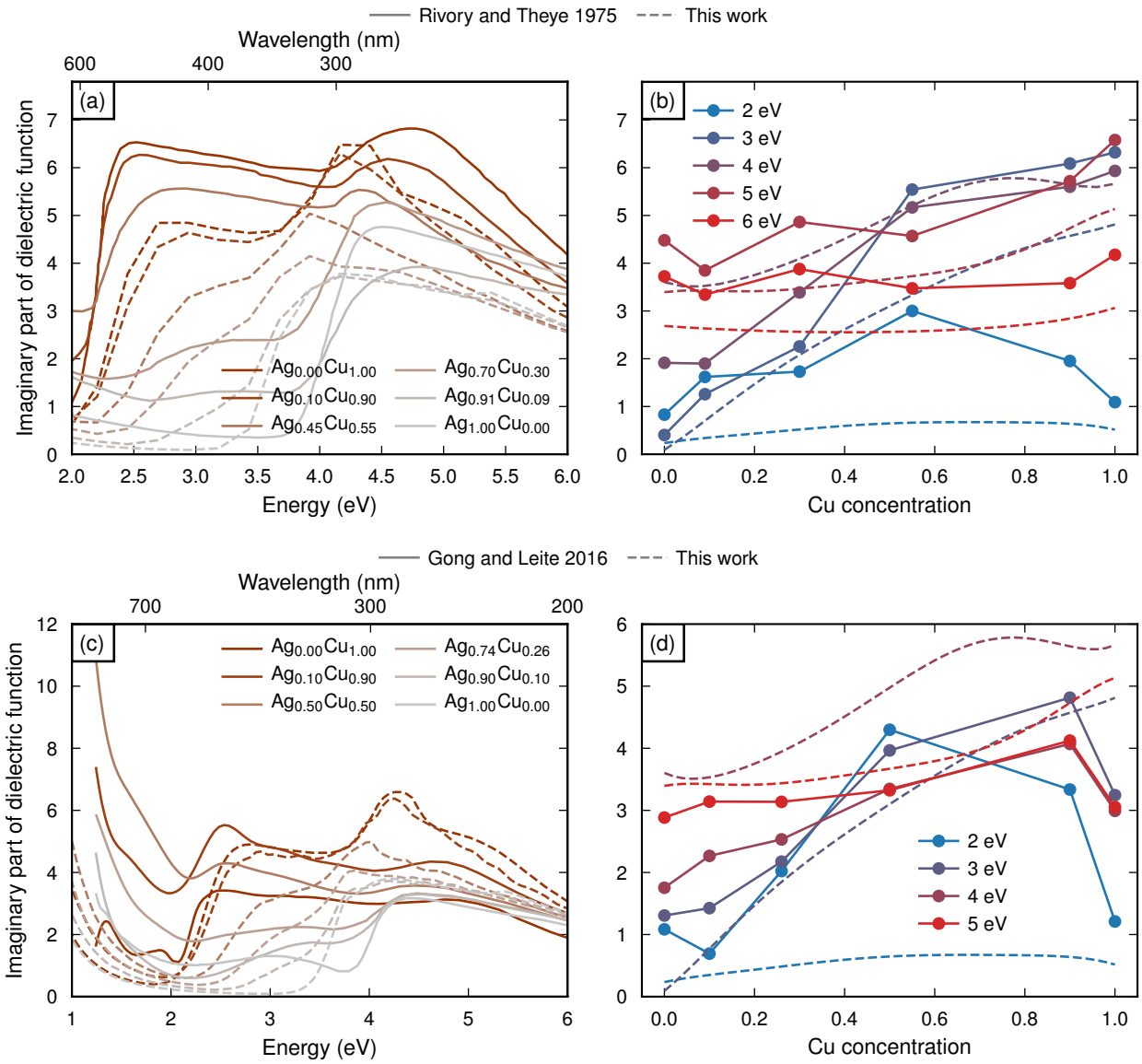

Figure S12: Comparison of Ag–Cu alloy dielectric functions to experimental data. Dielectric function of Ag–Cu, comparing our calculated DFs (dashed lines) to those of (24) (a–b) and (19) (c–d) as a function of photon energy (left) for all the concentrations presented in the respective references, and concentration (right) at specific photon energies.

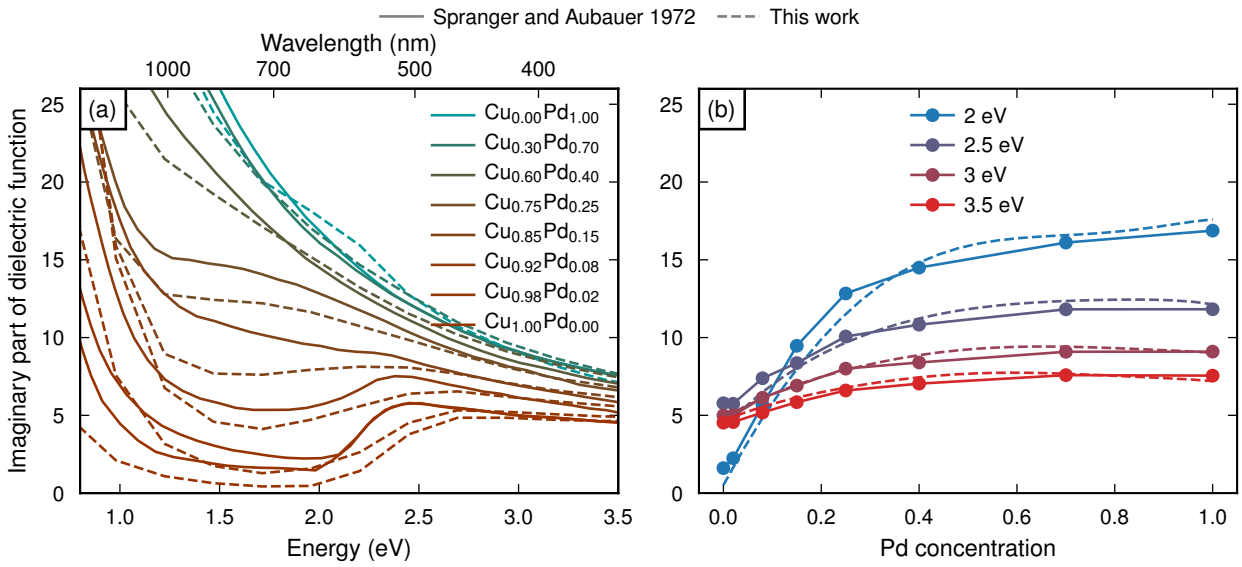

Figure S13: Comparison of Cu–Pd alloy dielectric functions to experimental data. Dielectric function of Cu–Pd, comparing our calculated DFs (dashed lines) to those of Ref. 25 (full lines, as reproduced in Ref. 22) as a function of (a) photon energy, for all the concentrations presented in Ref. 22, and (b) concentration at specific photon energies.

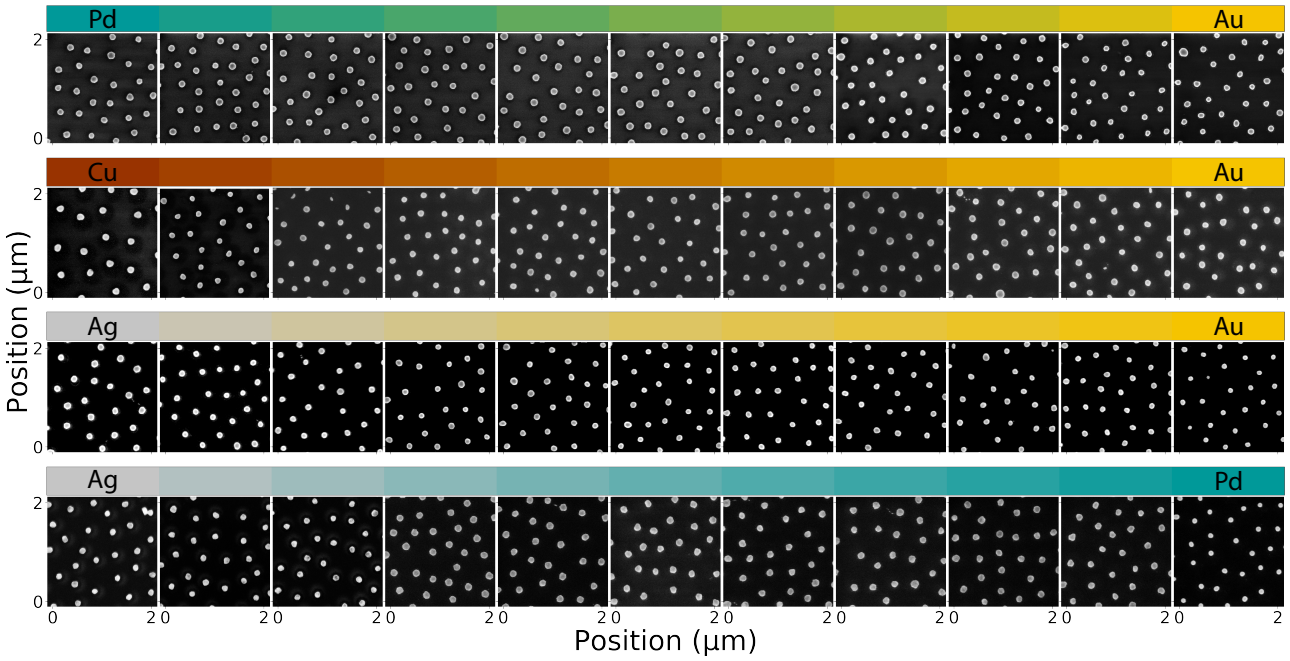

Figure S14: Overview of SEM images. Selected representative SEM images for each composition of the four experimentally assessed alloys, in steps of 10 at.-%. Such images were used to determine the mean diameter of the nanodisks in the experiment, which then was used for the corresponding FDTD simulation.

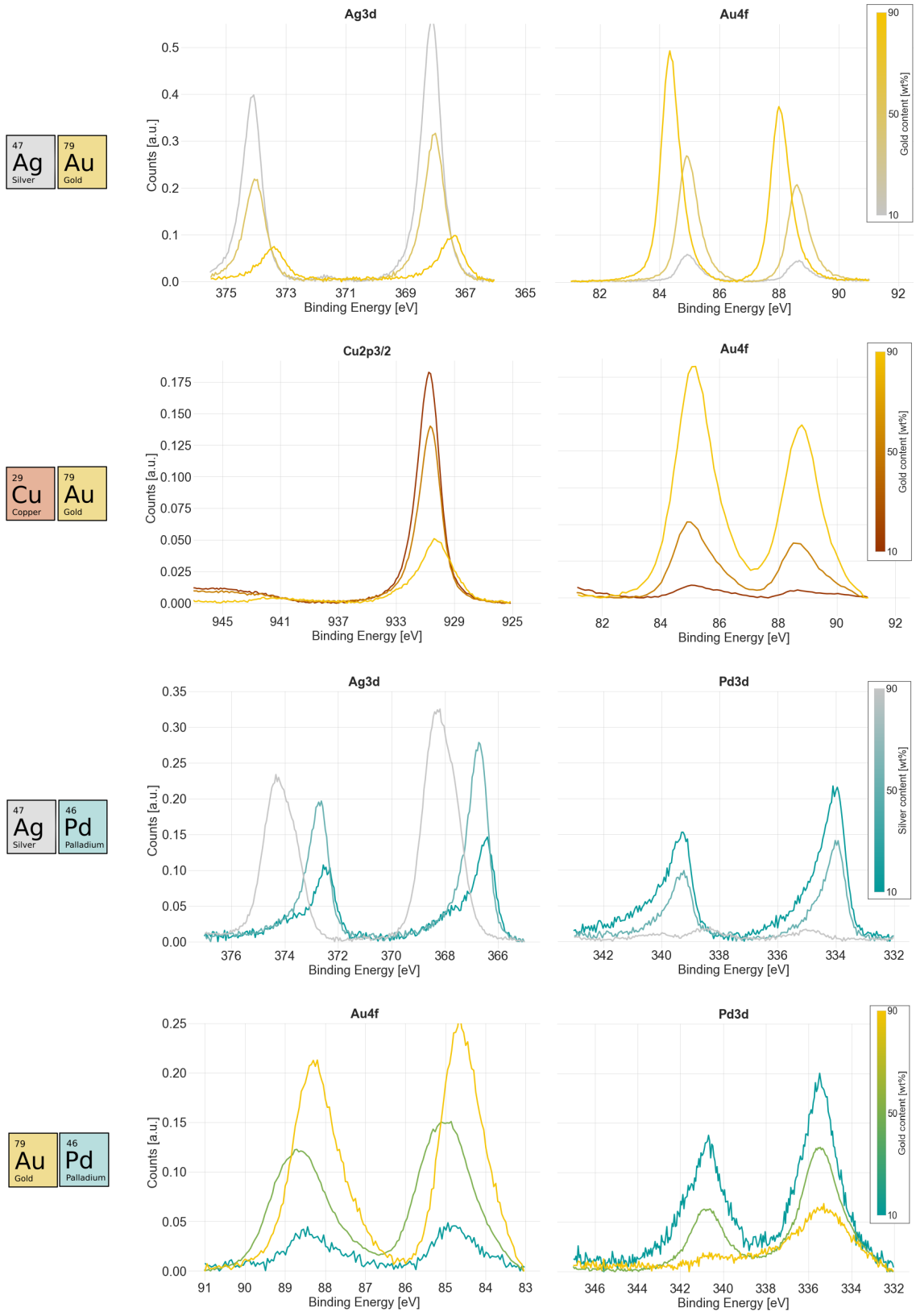

Figure S15: Overview of XPS measurements. Overview of XPS measurements of the four experimentally assessed alloys, each at concentrations of 10, 50 and 90 at.-%. A Shirley background was subtracted from all spectra. As the key observation we attribute the observed trends in binding energy peak shifts to the effect of alloying, in analogy to what has been reported for the Ag–Pd system in the literature (26).

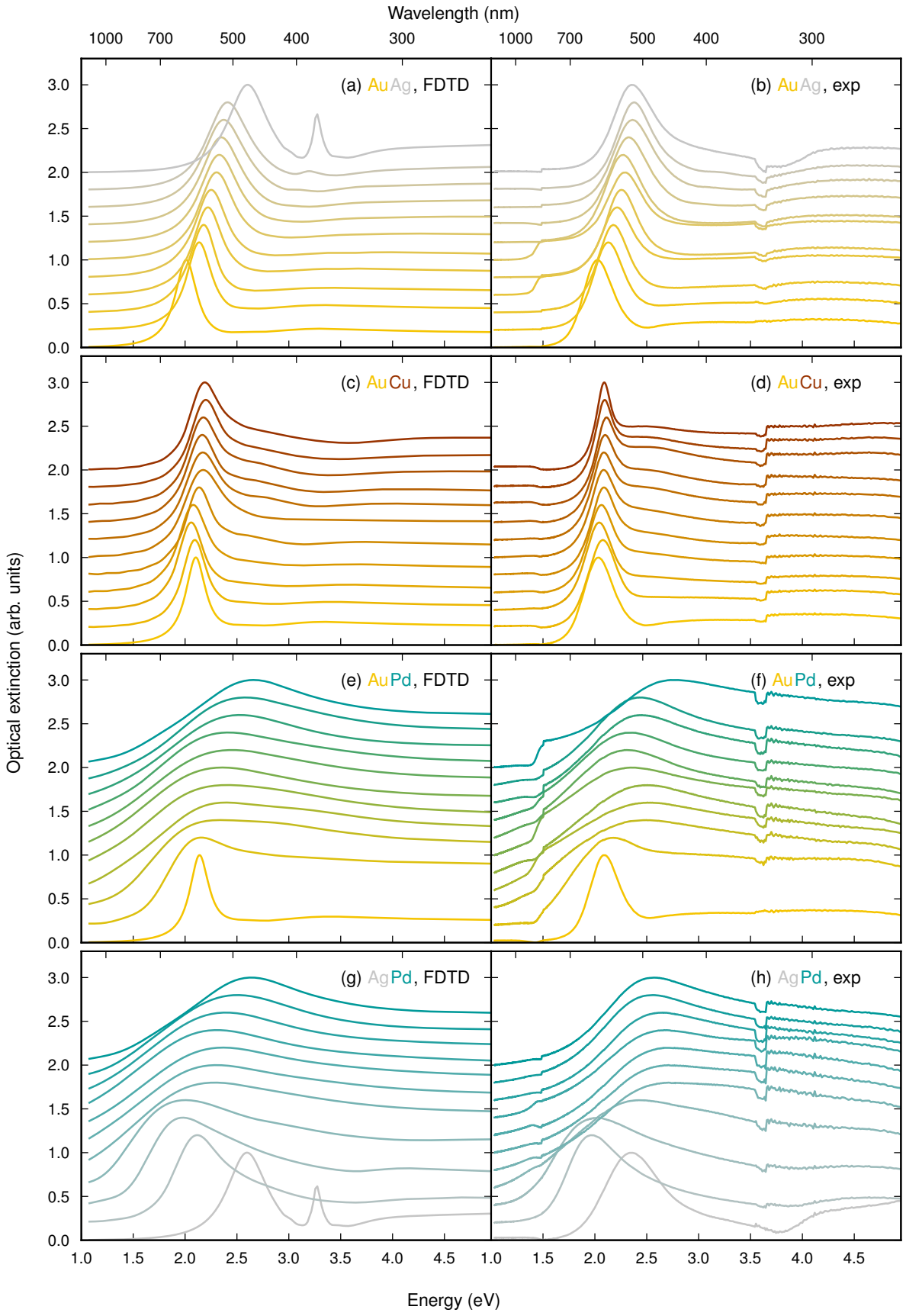

Figure S16: Optical extinction spectra of nanodisks. Extinction spectra as obtained with FDTD simulations using the dielectric functions calculated in this work (left), and experimentally by measuring extinction spectra of a quasi-random array of nanodisks (right), for Ag–Au (a–b), Au–Cu (c–d), Au–Pd (e–f), and Ag–Pd (g–h). The step-like feature at ca. 3.6 eV occurring in all experimental spectra is an artifact caused by the change of grating in the spectrophotometer. The additional peak at 3.3 eV in FDTD simulations of pure Ag is lacking in the corresponding experimental spectrum, probably due to ageing of the sample (see Fig. S17).

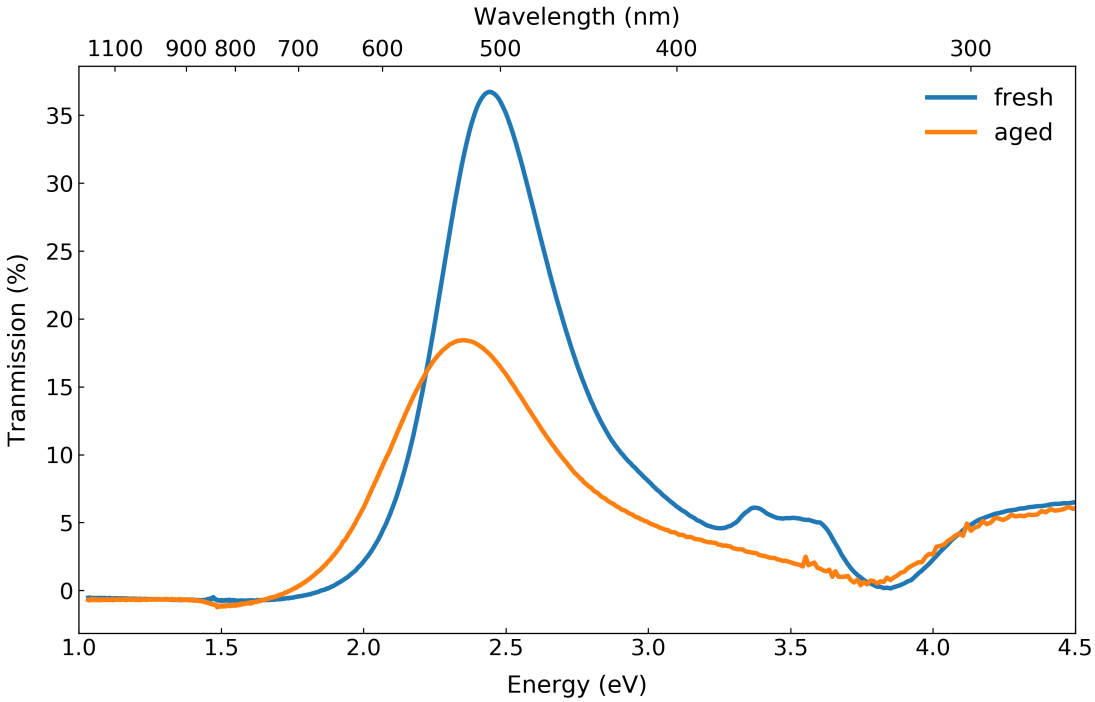

Figure S17: Spectra of fresh and aged nanodisks. Experimentally measured extinction spectra of a quasi-random array of pure Ag nanodisks before (blue) and after (orange) ageing in air for eight months, during which oxidation is likely to have occurred. Ageing redshifts and suppresses the plasmon peak, and the additional structure at approximately 3.5 eV is suppressed completely.

Supplementary References

[1] M. N. Polyanskiy, *Refractive index database,* https://refractiveindex.info. Accessed on 2019-12-16.

[2] S. Babar and J. H. Weaver, *Optical constants of Cu, Ag, and Au revisited,* Appl. Opt. **54**, 477 (2015). doi:10.1364/AO.54.000477.

[3] A. Ciesielski, L. Skowronski, M. Trzcinski, and T. Szoplik, *Controlling the optical parameters of self-assembled silver films with wetting layers and annealing,* Applied Surface Science **421**, 349 (2017). doi:10.1016/j.apsusc.2017.01.039.

[4] A. Ciesielski, L. Skowronski, M. Trzcinski, E. Górecka, P. Trautman, and T. Szoplik, *Evidence of germanium segregation in gold thin films,* Surface Science **674**, 73 (2018). doi:10.1016/j.susc.2018.03.020.

[5] H.-J. Hagemann, W. Gudat, and C. Kunz, *Optical constants from the far infrared to the x-ray region: Mg, Al, Cu, Ag, Au, Bi, C, and Al2O3,* J. Opt. Soc. Am. **65**, 742 (1975). doi:10.1364/JOSA.65.000742.

[6] P. B. Johnson and R. W. Christy, *Optical constants of the noble metals,* Phys. Rev. B **6**, 4370 (1972). doi:10.1103/PhysRevB.6.4370.

[7] P. B. Johnson and R. W. Christy, *Optical constants of transition metals: Ti, V, Cr, Mn, Fe, Co, Ni, and Pd,* Phys. Rev. B **9**, 5056 (1974). doi:10.1103/PhysRevB.9.5056.

[8] L. Gao, F. Lemarchand, and M. Lequime, *Comparison of different dispersion models for single layer optical thin film index determination,* Thin Solid Films **520**, 501 (2011). doi:https://doi.org/10.1016/j.tsf.2011.07.028.

[9] K. M. McPeak, S. V. Jayanti, S. J. P. Kress, S. Meyer, S. Iotti, A. Rossinelli, and D. J. Norris, *Plasmonic Films Can Easily Be Better: Rules and Recipes,* ACS Photonics **2**, 326 (2015). doi:10.1021/ph5004237.

[10] R. L. Olmon, B. Slovick, T. W. Johnson, D. Shelton, S.-H. Oh, G. D. Boreman, and M. B. Raschke, *Optical dielectric function of gold,* Phys. Rev. B **86**, 235147 (2012). doi:10.1103/PhysRevB.86.235147.

[11] M. A. Ordal, R. J. Bell, R. W. Alexander, L. L. Long, and M. R. Querry, *Optical properties of Au, Ni, and Pb at submillimeter wavelengths,* Appl. Opt. **26**, 744 (1987). doi:10.1364/AO.26.000744.

[12] M. R. Querry, *Optical Constants,* tech. rep., University of Missouri, Kansas City, Missouri, 1985.

[13] K. Stahrenberg, T. Herrmann, K. Wilmers, N. Esser, W. Richter, and M. J. G. Lee, *Optical properties of copper and silver in the energy range 2.5–9.0 eV,* Phys. Rev. B **64**, 115111 (2001). doi:10.1103/PhysRevB.64.115111.

[14] D. L. Windt, W. C. Cash, M. Scott, P. Arendt, B. Newnam, R. F. Fisher, and A. B. Swartzlander, *Optical constants for thin films of Ti, Zr, Nb, Mo, Ru, Rh, Pd, Ag, Hf, Ta, W, Re, Ir, Os, Pt, and Au from 24 Å to 1216 Å,* Appl. Opt. **27**, 246 (1988). doi:10.1364/AO.27.000246.

[15] Y. Wu, C. Zhang, N. M. Estakhri, Y. Zhao, J. Kim, M. Zhang, X.-X. Liu, G. K. Pribil, A. Alù, C.-K. Shih, and X. Li, *Intrinsic Optical Properties and Enhanced Plasmonic Response of Epitaxial Silver,* Advanced Materials **26**, 6106 (2014). doi:10.1002/adma.201401474.

[16] D. I. Yakubovsky, A. V. Arsenin, Y. V. Stebunov, D. Y. Fedyanin, and V. S. Volkov, *Optical constants and structural properties of thin gold films,* Opt. Express **25**, 25574 (2017). doi:10.1364/OE.25.025574.

[17] H. U. Yang, J. D'Archangel, M. L. Sundheimer, E. Tucker, G. D. Boreman, and M. B. Raschke, *Optical dielectric function of silver,* Phys. Rev. B **91**, 235137 (2015). doi:10.1103/PhysRevB.91.235137.

[18] W. Köster and R. Stahl, *Über den Einfluss von Legierungsbildung, Verformung und Rekristallisation sowie von Nah- und Fernordnung auf optische Konstanten der Edelmetalle und ihrer Legierungen,* Z. Metallkd. **58**, 768 (1967).

[19] C. Gong and M. S. Leite, *Noble Metal Alloys for Plasmonics,* ACS Photonics **3**, 507 (2016). doi:10.1021/acsphotonics.5b00586.

[20] O. Peña-Rodríguez, M. Caro, A. Rivera, J. Olivares, J. M. Perlado, and A. Caro, *Optical properties of Au-Ag alloys: An ellipsometric study,* Opt. Mater. Express **4**, 403 (2014). doi:10.1364/OME.4.000403.

[21] H. P. Myers, L. Walldén, and Å. Karlsson, *Some optical properties of CuPd, AgPd, AuPd and CuMn, AgMn alloys,* The Philosophical Magazine: A Journal of Theoretical Experimental and Applied Physics **18**, 725 (1968). doi:10.1080/14786436808227496.

[22] C. L. Foiles, *Chapter 4.7 Optical constants of binary alloys,* in *Landolt-Börnstein - Group III Condensed Matter 15B (Electrical Resistivity, Thermoelectrical Power and Optical Properties)*, edited by K.-H. Hellwege and J. L. Olsen (Springer-Verlag Berlin Heidelberg, 1985), p. . doi:10.1007/10201705_46.

[23] J. P. Ferraton, G. Leveque, and S. Robin-Kanadare, *Optical properties of silver-palladium alloys,* Journal of Physics F: Metal Physics **5**, 1433 (1975). doi:10.1088/0305-4608/5/7/023.

[24] J. Rivory and M. L. Theye, *Optical properties of Ag-Cu alloys : evidence for d-virtual bound states on Cu impurities,* J. Physique Lett. **36**, 129 (1975).

[25] H. Spranger and H. Aubauer, *Optische untersuchungen der elektronenstruktur ungeordneter und geordneter Cu-Pd Legierungen,* Journal of Physics and Chemistry of Solids **33**, 2113 (1972). doi:10.1016/S0022-3697(72)80241-5.

[26] K. H. Chae, Y. S. Lee, C. N. Whang, Y. Jeon, B. S. Choi, and M. Croft, *Charge redistribution in ion-beam-mixed Pd-Ag alloys,* Nuclear Instruments and Methods in Physics Research, Section B: Beam Interactions with Materials and Atoms **117**, 123 (1996). doi:10.1016/0168-583X(96)00293-5.